Copyright Undertaking

This thesis is protected by copyright, with all rights reserved.

By reading and using the thesis, the reader understands and agrees to the following terms:

1. The reader will abide by the rules and legal ordinances governing copyright regarding the use of the thesis.
2. The reader will use the thesis for the purpose of research or private study only and not for distribution or further reproduction or any other purpose.
3. The reader agrees to indemnify and hold the University harmless from and against any loss, damage, cost, liability or expenses arising from copyright infringement or unauthorized usage.

If you have reasons to believe that any materials in this thesis are deemed not suitable to be distributed in this form, or a copyright owner having difficulty with the material being included in our database, please contact lbsys@polyu.edu.hk providing details. The Library will look into your claim and consider taking remedial action upon receipt of the written requests.

Pao Yue-kong Library, The Hong Kong Polytechnic University, Hung Hom, Kowloon, Hong Kong

http://www.lib.polyu.edu.hk

The HONG KONG POLYTECHNIC UNIVERSITY

Characterisation of defects in hydrogenated Amorphous Silicon Thin Film

A THESIS

SUBMITTED

FOR THE DEGREE OF

MASTER OF PHILOSOPHY

by

Wai Yin Ho

July 1999

Pao Yue-Kong Library
PolyU • Hong Kong

Abstract

We report detailed characterization of thermal equilibration, metastability and light induced metastability in n-type hydrogenated amorphous silicon *a-Si:H* resistive devices. After the anneal, the samples were cooled at a rate of 0.5 K/s. Temperature dependencies of the low-frequency noise were studied from room temperature to about 420 K. The Arrhenius plots of voltage noise power spectra exhibit two different regimes separated by a kink at about 380K in their temperature dependencies. It is noted that the kink can be eliminated provided the subsequent cooling rate after the 450K annealing process is lowered to about 0.02 K/s. The characterization of the temperature dependencies of the device conductance exhibit the same equilibration temperatures as the flicker noise. Our experimental data provides strong evidence that the flicker noise originates from hydrogen motion within the material. In the second part of our experiments, the devices were exposed to 500W Xe lamp and HeCd laser. After the illumination, the Fouier Transform Infrared Spectroscopy (FTIR), Positron Annihilation Spectroscopy (PAS), and time dependencies of the low-frequency noise were studied. The experimental data showed that, the defect density of the sample decreased after illumination. It is suggested that the illumination, process led to light induced annealing effect.

Contents

1 Introduction **1**

2 Theory **4**

1 Spectral Analysis of Noise 4

1.1 $1/f$ Noise Theories 7

2 Fourier transform infrared spectroscopy 16

2.1 Theory of FTIR 16

2.2 Measurement methods 20

3 Positron annihilation spectroscopy 23

3.1 Positron beams system 24

3.2 Theory of PAS 27

3 Metastability in Hydrogenated Amorphous Silicon **33**

1 Staebler-Wronski Effect 35

2 Thermally Induced Metastability in Amorphous Silicon 38

3 Stretched exponential relaxation 40

4 Experiment **42**

1 $1/f$ noise measurement 42

1.1 Experimental setup 44

1.2 Sample preparation 45

2 Positron beam system 48

3 FTIR spectrometers 55

4 Experiment I : Low-frequency noise of thermal equilibration effects in *a-Si:H* 57

5 Experiment II : Low frequency noise and light induced Metastability . . . 58

5 Experimental Results **60**

1 DC conductivity 60

2 Low-frequency noise and Thermal equilibration effect 62

3 Results of low-frequency noise and light induced metastability in *a-Si:H* films 67

6 Discussion **76**

1 Thermal equilibration effect 76

2 Light induced metastability 80

7 Conclusion **84**

List of Figures

2.1 Infrared reflectance for a binary semiconductor, n-CdTe. Carrier concentration n in cm^{-3}: curve A, 5.1×10^{16}; curve B, 4.1×10^{17}; curve C, 1.3×10^{18}. Curve A shows nearly pure lattice response, with TO peak, and an LO minimum at $170 cm^{-1}$. As n increases, the minima at the coupled plasmon-phonon frequencies $\omega_{\pm}$ move to higher frequencies, and the low-frequency reflectance increases.[30] 19

2.2 Infrared reflectance for a ternary semiconductor. $Al_{0.14}Ga_{0.86}As$. Carrier concentration n in cm^{-3}: Curve A, 3.2×10^{18}; Curve B, 1.8×10^{18}. Curve C, 2.8×10^{18}; Curve D, 4.8×10^{18}. Curve A shows nearly pure lattice response with peaks at $270 cm^{-}1$ and $370 cm^{-1}$ from the GaAs-like and AlAs-like TO modes, respectively. Curves B,C, and D show increased low wave-number reflectance, and plasmon-phonon minima related to free carriers.[31] . . . 20

2.3 Michelson interferometer for transmissive FTIR spectroscopy. The black body illuminates the beam splitter (BS). The two resulting beams recombine in the interferogram signal $I(\Delta)$, where Δ is the difference in path length, which continues through the sample and to a detector. The computer performs a Fourier transform to recover intensity versus wavenumber. Reflectance can also be measured with a different geometry. 23

2.4 Definition of S and W parameters. The measured annihilation peak contains broadening caused by Doppler shift and instrumental resolution. A typical value for the windows are : for region A from 510.2 to 511.8 keV, for region B from 507.8 to 509.3 and from 512.7 keV to 514.8 keV, and for region C from 506to 516 keV 32

3.1 Energy-configuration diagrams for stable (a) and metastable structural configurations (b). Q and Q^* denote the ground state and excited states of the system, respectively. 34

3.2 Time decay of normalized light induced spin density for various temperatures. The solid circles are the data points while the solid lines are fits to the data using a stretched exponential time dependence.[50] 37

3.3 Time decay of the occupied band tail density n_{BT}, measured by the voltage pulse charge sweep-out technique, for various temperatures. 39

4.1 The experimental setup for low frequency noise measurement. 45

4.2 fabrication procedure for the Cr contact. 47

4.3 Coplanar electrode configurations used to measure noise frequency noise and conductance. 47

4.4 Magnetic transportation-general beam 51

4.5 Positron Gun Chamber. 52

4.6 Source and moderator. 53

4.7 Temporary target chamber. 54

4.8 Optical Path of sample holder 55

4.9 Model 16PC Optical System 56

4.10 Experimental setup for light induced degradation. 59

5.1 The I-V characteristics of the sample at room temperature. 61

5.2 The temperature dependence of conductance. 62

5.3 The noise power spectrum for five different current bias : a=$7\mu A$, b=$9\mu A$, c=$11\mu A$, d=$13\mu A$ and e=$15\mu A$ at room temperature. 63

5.4 The noise power for 200 Hz as a function of the bias current. 64

5.5 The noise power spectrum as a function of frequency for three different temperatures. 65

5.6 The Arrhenius plots of the conductance (curve A) and the voltage noise power spectral density measured at 200 Hz (curve B) after annealing followed by the rapid-cooling process. 66

5.7 The Arrhenius plots of the conductance (curve A) and the voltage noise power spectral density measured at 200 Hz (curve B) after annealing followed by the slow-cooling process. 67

5.8 The time dependence of conductance. Curve A shows the conductance of the sample during exposure to Xe lamp. Curve B shows the conductance of the sample after exposure. 68

5.9 The time dependence of noise power spectral density at 500 Hz for the sample after exposure to Xe lamp. 69

5.10 The time dependence of conductance for the sample after exposure to Xe lamp. 69

5.11 The exposure time dependence of conductance for the sample after exposure to HeCd laser illumination. 70

5.12 The exposure time dependence of noise power spectral density at 500 Hz for the sample after exposure to laser illumination. 71

5.13 IR transmission spectra for *a-Si:H* samples after annealing at 450 K (Curve A) and after the sample was exposed to Xe lamp illumination (Curve B). 72

5.14 IR transmission spectra for *a-Si:H* samples after annealed to 450 K (Curve A) and the sample was exposed to laser (Curve B). 74

5.15 S-parameter (S(E)) for the sample before exposed, after exposed, and annealing after exposed to Xe lamp. 74

5.16 S-parameter (S(E)) for the sample before exposed, after exposed, and annealing after exposed to HeCd laser. 75

6.1 $\text{Log}_{10}\, S_V(f = 200Hz)$ vs $\text{Log}_{10}R$. The data are obtained after the device have experienced thermal annealing at 450 K followed by the rapid-cooling process. 79

6.2 $\text{Log}_{10}\, S_V(f = 200Hz)$ vs $\text{Log}_{10}R$. The data are obtained after the device have experienced thermal annealing at 450 K followed by the slow-cooling process. 80

Chapter 1

Introduction

A turning point in the study of amorphous semiconductors was reached with the discovery that the addition of hydrogen to amorphous silicon could dramatically improve the material's optical and electrical properties. Hydrogenated amorphous silicon (*a-Si:H*) displays a photoconductive gain of over six orders of magnitude and its dark conductivity can be changed by over ten orders of magnitude by n-type or p-type doping [1]. Consequently, *a-Si:H* has become the material of choice for technological applications such as solar cells, input scanners and thin film transistors, which require the large surface area advantages of amorphous semiconductors. In addition, the relatively high electronic quality of *a-Si:H* has facilitated the study of the basic physics of amorphous semiconductors.

The role of hydrogen in *a-Si:H* is to passivate dangling bonds and modify the amorphous silicon network. Unhydrogenated amorphous silicon typically contains $\simeq 10^{19} cm^{-3}$ dangling bonds. In hydrogenated amorphous silicon, the density of dangling bond is $\simeq 10^{15} - 10^{16} cm^{-3}$ [2].

Hydrogen has been shown to diffuse quite easily in *a-Si:H* at moderate temperatures of $\simeq 200°C$. As hydrogen diffuses it breaks silicon hydrogen bonds, leaving behind new dangling bonds. On the other hand, hydrogen can form bond with an existing dangling bond, so it can passivate defect states. Thus motion of hydrogen motion in *a-Si:H* results in atomic rearrangement of the amorphous silicon structure and can lead to either defect removal or creation. Hydrogenated amorphous silicon displays various metastable effects, which are attributed to the motion of bonded hydrogen, these phenomena will be discussed in detail in the following chapters.

For detailed characterization of metastability in *a-Si:H* films, we performed systematic studies of $1/f$ noise, positron annihilation spectroscopy and FTIR spectroscopy on n-type *a-Si:H* film grown by plasma enhance chemical vapour deposition (PECVD).

There is a growing interest in the study of flicker noise in hydrogenated amorphous silicon thin films. Flicker noise is an important phenomenon of its own right as it represents the lower limit for signal processing. This is of particular significance for applications such as detectors and amplifiers. In addition, previous work shows that flicker noise can also be utilized as a sensitive tool for characterizing the reliability and the physical processes taking place within the device [3]-[7]. Recent work on low-frequency excess noise in n-type *a-Si:H* thin films and devices demonstrated Random telegraph Noise (RTN) in macroscopic *a-Si:H* samples of sub-millimeter dimensions. It was suggested that the motion of hydrogen atom may result in significant changes in the percolation path of the carrier which gives rise to the observed RTN [3]-[5]. Thus, flicker noise can also be used to characterize hydrogen motion in the material. In this thesis, we conduct extensive

studies to investigate the mechanism of the observed $1/f$ noise.

Much of the information about *Si-H* bonds come from Infrared absorption measurements. Hydrogen is a light atom, and since the phonon frequency is given by $(k/m)^{\frac{1}{2}}$, Where k is the force constant and m is the reduced mass, the frequencies of the hydrogen modes are above the silicon network modes, making then easy to observe. The vibration is almost entirely confined to the hydrogen atom, so that the analysis of the modes is relatively simple.

In recent years, positron annihilation has been used increasingly as a sensitive probe to low concentrations of open-volume defects sites, such as *Si* dangling-bond sites. In order to gain information about such defects it is necessary to moderate the energies of the positrons and then accelerate them to the desired implantation energy. Leo et al. measured Doppler broadening from *a-Si* and *a-Si:H* relative to crystalline *Si* using a positron source without any depth resolved information [8]. The average S parameters for *a-Si* and *a-Si:H* were 1.02 and 1.007, respectively, showing the influence of hydrogen on measured S values. The S value of *a-Si* falls after adding hydrogen, suggesting that the density of positron trap centers is reduced. Thus, we conduct extensive studies of positron annihilation to investigate the dangling-bond density in *a-Si:H*.

Chapter 2

Theory

1 Spectral Analysis of Noise

Signals are most commonly represented as a time-varying quantity such as a voltage $v(t)$. This perspective is reinforced by the easy observation of this signal using an oscilloscope. However, the same information can be presented by a spectrum $F(\omega)$, and the display and direct measurement of the frequency content of a signal is possible with a spectrum analyzer.

Although equivalent information is presented in the display of the signal as a function of time and as a function of frequency, the visualization or analysis of a particular information may be much easier in one representation than the other. It is almost only by chance that oscilloscopes were developed before spectrum analyzers and that we are accustomed to think mainly in the time domain. In many instances the representation of a signal by its frequency content using Fourier transform is a useful technique for characterizing its statistical properties.

Noise in semiconductors, like any other stochastic process, is characterized by its statistical properties, which often reveal the underlying physics. An important statistical function for noise study is the power spectral density which for a random variable $x(t)$ is defined as [9]

$$S_X(f) = \lim_{T\to\infty} \frac{2\left|X_T(f)\right|^2}{T}, \tag{2.1}$$

where $X_T(f)$ is the fourier transform of $x_T(t)$,

$$x_T(t) = \begin{cases} x(t), & -T/2 \le t \le T/2, \\ 0, & \text{otherwise.} \end{cases} \tag{2.2}$$

The power spectral density has the unit of $[x]^2/Hz$. To show that $S_X(f)$ does represent the average power per bandwidth for x_T, we apply Parseval's theorem which relates any two time-varying functions $x_1(t)$ and $x_2(t)$ to their Fourier transforms $X_1(f)$ and $X_2(f)$ as the following:

$$\int_{-\infty}^{\infty} dt x_1(t) x_2^*(t) = \int_{-\infty}^{\infty} df X_1(f) X_2^*(f), \tag{2.3}$$

where the asterisks denote complex conjugates. Replacing both $x_1(t)$ and $x_2(t)$ with $x_T(t)$ and dividing Eq.2.3 by T, we get

$$\frac{1}{T}\int_{\frac{-T}{2}}^{\frac{T}{2}} dt x_T^2(t) = \int_{-\infty}^{\infty} df \frac{\left|X_T(f)\right|^2}{T}, \tag{2.4}$$

The right side of Eq.2.4 can be identified as the average power of $x(t)$. Since $x_T(t)$is real, the magnitude of $X_T(f)$ is an even function. Restricting the frequency to only positive values and taking the limit of Eq.2.4 as T goes to infinity, we complete the proof,

$$\int_0^{\infty} df X_T(f) = \lim_{T\to\infty}\int_0^{\infty} df \frac{2\left|X_T(f)\right|^2}{T} = \lim_{T\to\infty}\frac{1}{T}\int_{-\frac{T}{2}}^{\frac{T}{2}} dt X_T^2(t), \tag{2.5}$$

For theoretical analysis of noise, we often compute the auto-correlation function, which indicates the memory of the stochastic process and is defined as Eq.2.5 [9]

$$\Phi_x(t) \equiv \langle x(\tau)x(\tau+t)\rangle = \lim_{T\to\infty}\frac{1}{T}\int_{-\frac{T}{2}}^{\frac{T}{2}} d\tau x(\tau)x(\tau+t), \tag{2.6}$$

where the brackets denote ensemble average. Where the assumption of ergodicity holds, the ensemble average is replaced with a time average. Then the Fourier transform of $\Phi(\tau)$ is

$$\mathcal{F}\{\Phi(t)\} = \int_{-\infty}^{+\infty} R(\tau)e^{-j\omega\tau}d\tau = 2\pi S_X(\omega), \tag{2.7}$$

where $\mathcal{F}$ is the Fourier Transformation operator. Hence, the inverse Fourier transform of Eq. 2.7 is given as

$$\Phi(\tau) = \int_{-\infty}^{+\infty} S_X(\tau)e^{j\omega\tau}d\omega, \tag{2.8}$$

where $-\infty < \omega < \infty$ Since $\Phi(\tau)$ is a real and even function, then from Eq. 2.7, we have

$$\begin{aligned}\mathcal{F}\{\Phi(\tau)\} &= 2\int_0^{\infty}\Phi(\tau)e^{-jw\tau}d\tau,\\ &= 2\int_0^{\infty}\Phi(\tau)\cos(\omega\tau)d\tau,\end{aligned} \tag{2.9}$$

However, from Eq. 2.8, one can get

$$\mathcal{F}\{\Phi(\tau)\} = 2\pi S_X(\omega), \tag{2.10}$$

where $-\infty < \omega < \infty$ As a result,

$$S_X(\omega) = \frac{2}{\pi}\int_0^{\infty}\Phi(\tau)\cos(\omega\tau)d\tau, \tag{2.11}$$

In order to change variable ω to f, let's refer to Eq. 2.8,

$$\begin{aligned}\Phi(\tau) &= \int_{-\infty}^{+\infty} S_X(\omega)\cos(\omega\tau)d\omega,\\ &= \int_{-\infty}^{+\infty} S_X(f)\cos(2\pi f\tau)df,\end{aligned} \tag{2.12}$$

where $d\omega = 2\pi df$, one can get

$$S_X(f) = 4\int_0^\infty \Phi(\tau)\cos(2\pi f\tau)d\tau, \tag{2.13}$$

According to Eq. 2.12, one can obtain

$$\Phi(\tau) = \frac{1}{2\pi}\int_0^\infty S_X(f)\cos(2\pi f\tau)df, \tag{2.14}$$

Equations 2.13 and 2.14 is the $Wiener - Khintchine$ relationship [10]. This relationship is used extensively for determining the power spectral density of a continuous random signal.

1.1 $1/f$ Noise Theories

Introduction

Flicker noise was first observed by Johnson in 1925. Since then it has become a subject of much research interest. This type of noise presents one of the most interesting phenomena in physical systems [11]-[16]. Peculiar aspects of the phenomenon include :

1. The wide range of systems exhibiting $1/f$ like fluctuation, including metals semiconductors, biological systems, stock market, music, etc.,
2. The apparent lack of cut-off frequencies for the $1/f$ spectrum.

The study of flicker noise is important because the noise reflects the underlying physical mechanism of electrical conduction. For electron devices, the investigation of $1/f$

noise is an important subject of its own right. It represents the lower limit of the signal that can be processed by the device. Also because of the shape of the noise power spectral density, flicker noise is the dominant type of fluctuation in the low frequency regime typically for $f<10$ kHz. This represents a severe limitation to the sensitivity of the device in processing small signals. An understanding of the origin of flicker noise is required before one can systematically to lower or even to eliminate the noise in the system.

In the following sections we will present a brief outline of the existing models for low frequency excess noise.

Hooge's Empirical Model

This is an empirical model proposed by Hooge in 1969 [17]. He performed a systematic study on the experimental results of $1/f$ noise in various systems and found that the power spectra of the low frequency excess noise from a wide range of materials, both metallic and semiconductor, could be expressed by and empirical equation

$$\frac{S_I(f)}{I^2} = \frac{\alpha_H}{N_c f}, \tag{2.15}$$

Where α_H is a dimensionless constant, commonly know as the Hooge parameter, equals 2×10^{-3} and N_c is the number of free carriers in the sample. Equation 2.15 implies that the current noise power spectral density is directly proportional to the number of free carrier. This implies that the total noise power spectrum is the linear superposition

of noise power spectra of individual electrons, each with a $1/f$ dependence. To give physical interpretation for the spectral shape, Hooge and Vandamme [18] postulated that $1/f$ noise arises from fluctuations in the phonon scattering of mobile carriers. The model received support from work by R.Jindal and A.van der Ziel [19] who calculated $1/f$ noise power spectrum from fluctuations in the occupancy of phonon modes, where each carrier interacted with only a subset of phonon modes.

Despite the wide use of the Hooge's equation, critics of the model reject Hooge's formula and its interpretation on the following grounds:

1. While the Hooge's equatuion is consistent with noise data taken on a number of metals and semiconductors, samples with α_H differing from 2×10^{-3} by orders of magnitude have been reported, casting doubt on the existence of a universal formula;
2. Typical time scales of phonon scattering, on the order of picoseconds, are incompatible with the fact that the $1/f$ spectrum extends to frequency as low as 10^{-6} Hz;
3. The spectral slopes (in logarithmic scales) often are not exactly -1, as is required by Eq. 2.15, but range form -0.8 to -1.4 which change with temperature.

The quantum $1/f$ noise theories

Another attempt to give physical meanings to the Hooge equation is the formulation of the quantum $1/f$ noise to mobility fluctuations [16][20][21]. Handel proposed a different

origin of mobility fluctuations: interactions of scattered charges with the electromagnetic field, which in turn modulates the scattering process [20]. Unlike defect-related noises, quantum $1/f$ noise based on the quantum nature of matter, are fundamental, and thus cannot be avoided with improvements in technologies.

Values of the Hooge parameter, α_H, computed for quantum $1/f$ noise are of the order of 10^{-9} to 10^{-8} when intervalley scattering processes are not involved [15], and of the order of 10^{-6} to 10^{-5} when intervalley scattering processes are involved. While experimental values of α_H over the above ranges have been obtained [15][22], the computed values fail to explain the large number of samples exhibiting α_H on the order of 10^{-3}. In view of such discrepancies, Handel proposed a different quantum process: coherent state quantum $1/f$ fluctuations [23]. Calculations based on such mechanism predict a $\alpha_H = 4.65 \times 10^{-3}$ in good agreement with the high experimental range of α_H.

Hooge, however, argued [24] that experiments devised for verification of quantum $1/f$ processes were not conclusive, since the only quantity to measured was α_H, and thus one could not rule out other possible noise processes. Like Hooge's model, Handel's theories are applicable only to cases where the noise exhibits a strictly $1/f$ spectrum, i.e. with a slope of -1 [16]. The abundant amount of data where the spectral slopes deviate from -1, clearly indicates that in many samples the Hooge-type processes are not the dominant source for $1/f$ noise. In those cases, quantum $1/f$ fluctuations may be present but are overwhelmed by fluctuations of different origins.

Thermal Activation Model

The power spectrum of a random process, characterized by a single relaxation time, is a lorentzian, $C\tau_T/(1+4\pi^2f^2\tau_T^2)$, which has a distinct corner frequency $f_c = 1/2\pi\tau_T$, where C is a proportionality constant and τ_T is the fluctuation time constant. Bernamont first noted that the superposition of many Lorentzians with a distribution of τ_T would give rise to a more gradual spectrum [16][25]. He showed that if the relaxation time is thermally activated

$$\tau_T = \tau_0 exp(\frac{E_\tau}{k_BT}), \tag{2.16}$$

where E_τ is the activation energy, then a uniform distribution of E_τ, $D(E_\tau)$, at around E_0, would give an exact $1/f$ spectrum within a lower and an upper frequency limits, provided the Lorentzian prefactor C remained a constant over E_τ [26]

$$\begin{aligned} S_V(f) &= \int D(E_\tau)\frac{C\tau_T(E_\tau)}{1+4\pi^2f^2\tau_T^2(E_\tau)}dE_\tau, \\ &\simeq \frac{CD_0}{4f}, \end{aligned} \tag{2.17}$$

for $1/2\pi\tau_1 \ll f \ll 1/2\pi\tau_2$, where τ_1 and τ_2 are the lower and the upper limits of τ_T respectively. Following Bernamont [25] and Surdin [26], Dutta and Horn [12] condsidered $1/f$ noise resulting from the superposition of Lorentzian spectra arising from thermally activated processes, where the required distribution of τ_T resulted form a distribution of E_τ. Dutta et al. found that a smooth $D(E_\tau)$ on the scale of k_BT would give rise to a spectral density varying as $1/f^\gamma$, where $\gamma \approx 1$.

Since both the spectral slope $-\gamma$ and the magnitude of the noise power spectra depend on the distribution of $D(E_\tau)$, a relationship can be derived connecting the two measurable quantities. For the Lorentzian factor $\tau_T(E_\tau)/(1 + 4\pi^2 f^2 \tau_T^2(E_\tau))$ is a sharply peaked function of activation energy with peak E_p. Since $\tau_T = \tau_0 \exp(E_\tau/k_B T)$, Lorentzian factor is then given by

$$L_F = \frac{\tau_0 exp(E_\tau/k_B T)}{1 + 4\pi^2 f^2 \tau_0^2 \exp(2E_\tau/k_B T)}, \tag{2.18}$$

It can be shown that the Lorentzian peaks at $4\pi^2 f^2 \tau_0^2 \exp(2E_\tau/k_B T) = 1$. We obtain

$$E_p = -k_B T \ln(2\pi f \tau_0), \tag{2.19}$$

From Eq. 2.19, we note that one effectively probes traps with different activation energies by measuring the noise power spectral at different temperatures and frequencies. In addition, the logarithmic dependence of E_p on the frequency, f, explains the weak dependence of γ on frequency in flicker noise.

At a given temperature and frequency, and for a smoothly varying $D(E_\tau)$ around energy E_p, we obtain the following relationship:

$$S_V(f) = C \int D(E_p) \frac{\tau_T}{1 + 4\pi^2 f^2 \tau_T^2} dE = C D(E_p) \frac{k_B T}{4f}, \tag{2.20}$$

From Eq. 2.20, one can express the distribution function in terms of $S_V(f)$:

$$D(E_p) = \frac{4f S_V(f)}{C k_B T}, \tag{2.21}$$

It is evident from Eq. 2.21 that the shape of $D(E_\tau)$ directly affects the magnitude and the spectral form of noise. Varying both f and T while keeping E_p unchanged, Dutta et al. Derived the following relation from Eq. 2.19 and 2.21

$$(\Delta f\frac{\partial}{\partial f}+\frac{\Delta T\partial}{\partial f})[-k_BT\ln(2\pi f\tau_0)]=0, \quad (2.22)$$

$$(\Delta f\frac{\partial}{\partial f}+\frac{\partial}{\partial f})[\frac{4fS_V(f)}{Ck_BT}], \quad (2.23)$$

For simplification reason we transfer the above two equations to below style respectively:

$$\Delta\omega\frac{\partial}{\partial\omega}+\Delta T\frac{\partial}{\partial T}[\omega S_V(\omega,T)/k_BT]=0, \quad (2.24)$$

$$\Delta\omega\frac{\partial}{\partial\omega}+\Delta T\frac{\partial}{\partial T}[k_BT\ln(\omega\tau_0)]=0, \quad (2.25)$$

From Eq. 2.24 we get

$$\Delta\omega\frac{S_V(\omega,T)}{kt}+\frac{\omega\Delta\omega}{kT}\frac{\partial TS_V(\omega,T)}{\partial\omega}-\Delta T\frac{\omega S_V(\omega,T)}{kT^2}+\Delta T\frac{\omega}{kT}\frac{\partial S_V(\omega,T)}{\partial T}=0, \quad (2.26)$$

then

$$\Delta\omega\frac{\omega}{S_V}\frac{\partial S_V}{\partial\omega}=\frac{\Delta T\omega}{T}-\frac{\Delta T\omega}{S_V}\frac{\partial S_V}{\partial T}-\Delta\omega, \quad (2.27)$$

From Eq. 2.25 we get

$$\Delta\omega kT\frac{1}{\omega}+\Delta Tkln(\omega\tau_0)=0, \quad (2.28)$$

so

$$\Delta T=-\frac{1}{ln(\omega\tau_0)}\frac{\Delta\omega T}{\omega}, \quad (2.29)$$

Then

$$\begin{aligned}\gamma &= 1+\frac{\omega}{\Delta T}\frac{1}{ln(\omega\tau_0)}\frac{\Delta\omega T}{\omega}-\frac{1}{ln(\omega\tau_0)},\frac{\Delta\omega T}{\omega}\frac{\omega}{\Delta\omega S_V}\frac{\partial S_V}{\partial T}\\ &= 1-\frac{1}{ln(\omega\tau_0)}(\frac{\partial lnS_V}{\partial lnT}-1),\\ &= 1-\frac{1}{ln(2\pi f\tau_0)}(\frac{\partial lnS_V}{\partial lnT}-1), \quad (2.30)\end{aligned}$$

So we can relate the spectral shape to the temperature dependence of the spectral (Dutta-Horn relation):

$$\gamma = \frac{\partial lnS_V}{\partial lnf} = 1 - \frac{1}{ln(2\pi f\tau_0)}(\frac{\partial lnS_V}{\partial lnT} - 1). \tag{2.31}$$

The Dutta-Horn relation, Eq. 2.30, provides a self-consistency test of the thermal activation model. From their studies of $1/f$ noise in metal films resistors, they found that the relation Eq. 2.30 agreed well with the experimental data below 670 K. Extensive work following the discovery indicates that the fluctuation processes in metal film are associated with thermally activated diffusion of defects.

The McWhorter Model

Flicker noise in metal-oxide-semiconductor (MOS) systems, according to McWhorter [27], originates from carrier trapping by localized states in the oxide in the form of number fluctuations. Fluctuations in the charge state of an oxide trap in the process of random capture and emission of carriers modulate the local Fermi level at the semiconductor surface, thereby causing fluctuations in the number of mobile carriers, which in turn lead to fluctuations in the conductivity σ

$$\Delta\sigma = e\mu\Delta n, \tag{2.32}$$

where the mobility μ is assumed to be constant.

The statistics of number fluctuations due to carrier trapping are calculated by considering the kinetic rates of the oxide traps, which differ from those of semiconductor

bulk traps in that the oxide traps are spatially separated from the carriers. In the model, trapping and detrapping of carriers take place via tunneling. Therefore [28]

$$g_n = e_n n_T exp(-kz), \tag{2.33}$$

$$r_n = c_n n(N_T - n_T) exp(-kz), \tag{2.34}$$

where the exponential factor is the tunneling probability, k is the WKB parameter, and z is the distance of the trap from the semiconductor surface. So the power spectrum for fluctuations in the trap occupancy in an elemental volume $\Omega = \Delta x \Delta y \Delta z$ is

$$S_{\Delta N}(f) = 4N_{TT}(E,z) f_T(1-f_T)\Delta x \Delta y \Delta z \Delta E \frac{\tau}{1+4\pi^2 f^2 \tau_T^2} \tag{2.35}$$

where $N_{TT}(E,z)$ is the density of traps in $cm^{-2}eV^{-1}$ and

$$\begin{aligned} \tau_T &= \frac{1}{c_n[(N_T - n_T) + n + n_s]} exp(kz) \\ &\equiv \tau_0 exp(kz) \end{aligned} \tag{2.36}$$

The Fermi factor $f_T(1-f_T)$ in Eq. 2.35 as a function of the trap energy E_T peaks sharply at $E_T = E_F$. Therefore, only traps with energies within a few $k_B T$ from the Fermi level contribute to number fluctuations.

We observe that Eq. 2.36 that τ_T varies exponentially with the tunneling distance, the required distribution of τ_T for a $1/f$ spectrum can be obtained from the spatial distribution of traps in the oxide. It has been shown that a slowly varying N_{TT} gives rise to a $1/f^\gamma$ spectrum, with γ close to 1. In the case where N_{TT} is constant over z, a strictly $1/f$ spectrum is obtained.

Surya et al. [29] showed that any non-uniformity in $N_{TT}(E,z)$ would cause the spectral slope to deviate from the value one and vary over different gate biases. Approximating $N_{TT}(E,z)$ locally with an exponential

$$N_{TT}(E,z) = N + Toexp(-\xi|E| + \eta z), \tag{2.37}$$

where ξ and η are two constants, the spectral slope $-\gamma$ can be shown to be a function of the gate bias V_g

$$-\gamma = -(1 - \frac{e(|V_g - V_d|)\xi}{kt_{ox}} + \frac{\eta}{k}), \tag{2.38}$$

where V_d is the drain bias, and $t_o x$ is the oxide thickness. In studying the dependence of noise in p-channel MOSFETs on the gate bias and the temperature, Surya et al. [29] found that the McWhorter model could not adequately explain the experimental data, in particular, the strong temperature dependence of γ. The data could be accounted for, however, by a model in which the trap kinetics were governed by thermally activated processes, instead of by tunneling processes. Recent measurements of RTN due to individual trapping events provide the strongest evidence that such capture and emission of carriers are indeed thermally activated.

2 Fourier transform infrared spectroscopy

2.1 Theory of FTIR

The linear diatomic chain model for a binary semiconductor also gives the lattice dielectric function $\epsilon_{lat}(\omega)$. Under an applied electric field $E = E_0 e^{-i\omega t}$ and assuming a frictional force proportional to velocity, the displacement u of the positive ions relative to the

negative ones is :

$$u \propto \frac{E_0 e - i\omega t}{\omega_{TO}^2 - \omega^2 - i\Gamma\omega} \tag{2.39}$$

where the term ω_{TO}^2 comes from the spring restoring force, and Γ is the strength of the frictional term. This gives the polarization vector P according to the definition :

$$P = Nqu \tag{2.40}$$

where N is the number of ion pairs per cubic centimeter and q is the ionic charge. Then, the lattice dielectric function $\epsilon(\omega)$ in the semiconductor takes the from :

$$\epsilon_{lat}(\omega) = (n + ik)^2 = \epsilon(\infty) + \frac{S\omega_{TO}^1}{\omega_{TO}^2 - \omega^2 - i\Gamma\omega} \tag{2.41}$$

The constant $\epsilon(\infty)$, the high frequency limit of $\epsilon_{lat}(\omega)$, comes from the deeply bound valence electrons whose frequency response is flat in the infrared. The oscillator strength U is proportional to N. It is related to the static dielectric constant at zero frequency $\epsilon(0)$ and the high frequency dielectric constant $\epsilon(\infty)$ by :

$$\epsilon(0) = \epsilon_{lat}(0) = \epsilon(\infty) + U \tag{2.42}$$

Eq. 2.41 is the Lorentzian from for the infrared lattice response, which is also useful for local vibrational modes induced by impurities. Its physical meaning is clear in the ideal case without damping, with $\Gamma = 0$. It becomes

$$\epsilon_{lat}(\omega) = \epsilon(\infty) + \frac{U\omega_{TO}^2}{\omega^2 TO - \omega^2} \tag{2.43}$$

which resonates at $\omega = \omega_{TO}$. Equally important, $\epsilon_(\omega)$ becomes zero and hence supports a longitudinal mode at the longitudinal optical frequency ω_{LO}. The condition $\epsilon_{lat}(\omega) = 0$

gives :

$$\frac{\omega_{LO}^2}{\omega_{TO}^2} = \frac{\epsilon(0)}{\epsilon(\infty)} \tag{2.44}$$

which is the well-known Lyddane-Sachs-Teller relation. Since $\epsilon(0) \gg \epsilon(\infty)$, $\omega_{LO} \gg \omega_{TO}$, an increase due to the macroscopic electric field associated with the longitudinal oscillations. Separate TO and LO modes exist in binary material; both are important in infrared and Raman scattering. For the covalent group IV semiconductors, the oscillator strength $U = 0$; hence $\epsilon(0) = \epsilon(\infty)$ and $\omega_{LO} = \omega_{TO}$ at zero wave-vector.

When n and k are derived from Eq. 2.41, the result is a peak in the reflectance very nearly at ω_{TO}. The peak value is $R = 1$ in the ideal undamped case, and very high even for real semiconductors, where the damping term Γ_ω is small. A second important feature in the reflectance spectrum is the minimum in R when $n = 1$, which is very nearly the condition $n = 0$ which defines ω_{LO}. The maximum at ω_{TO} and minimum at ω_{LO} are key features in the interpretation of infrared reflectance spectra, but there is a fundamental physical difference. The peak marks resonant absorption of the incident radiation, whereas the minimum indicates the presence of a longitudinal mode without resonant absorption. Curve A in Fig 2.1 displays R versus ω for a bulk semiconductor with few carriers, clearly showing the lattice TO and LO features.

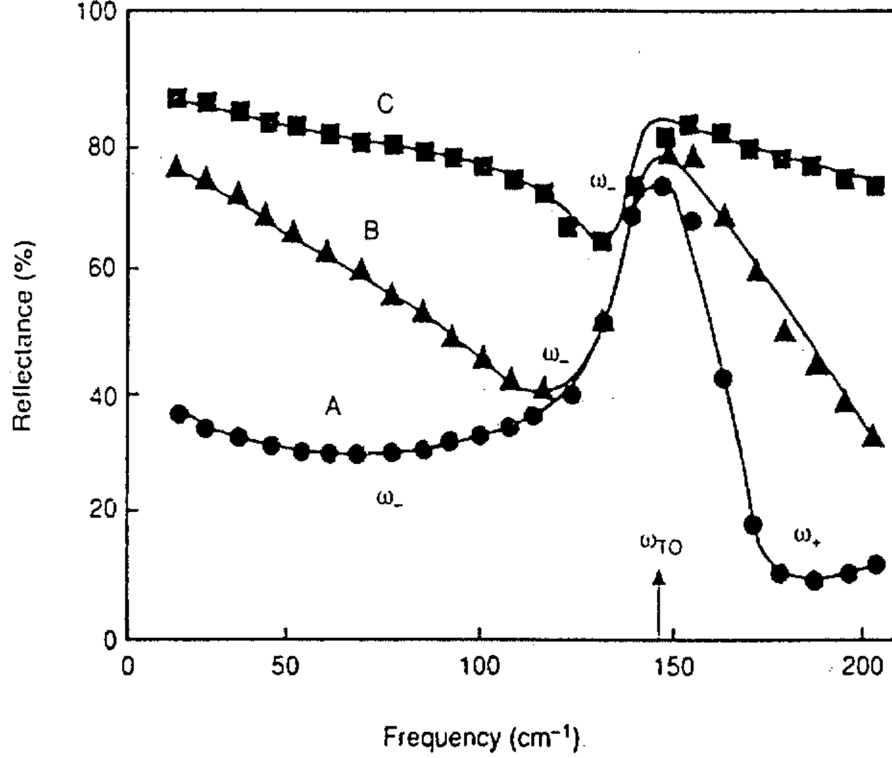

Figure 2.1: Infrared reflectance for a binary semiconductor, n-CdTe. Carrier concentration n in cm^{-3}: curve A, 5.1×10^{16}; curve B, 4.1×10^{17}; curve C, 1.3×10^{18}. Curve A shows nearly pure lattice response, with TO peak, and an LO minimum at $170 cm^{-1}$. As n increases, the minima at the coupled plasmon-phonon frequencies $\omega_{\pm}$ move to higher frequencies, and the low-frequency reflectance increases.[30]

For a ternary or quaternary alloy, Eq. 2.41 may be extended to include the effects of the oscillation sub-lattices in the from:

$$\epsilon_{lat}(\omega) = \epsilon(\infty) + \sum_{j=1}^{J} \frac{S_j \omega_{TOj}^2}{\omega_{TOj}^2 - \omega^2 - i\Gamma_j \omega} \tag{2.45}$$

where J is the number of sub-lattices, each with its won TO frequency, oscillator strength, and damping constant. This multiple resonance form describes $Al_{1-x}Ga_xAs$ and $Hg_{1-x}Cd_xTe$, for instance. Curve A in Fig 2.2 shows reflectance for an $Al_{1-x}Ga_xAs$ sample with few carriers, illustrating the two lattice TO modes. The intensities and frequencies of the peaks shift with x, giving a useful characterization tool.

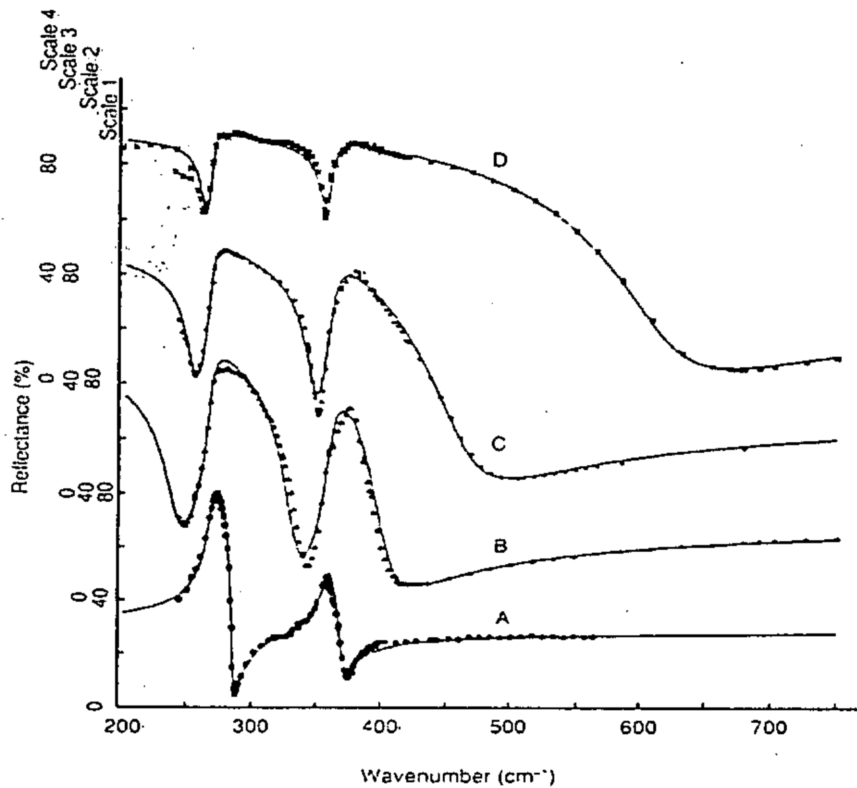

Figure 2.2: Infrared reflectance for a ternary semiconductor. $Al_{0.14}Ga_{0.86}As$. Carrier concentration n in cm^{-3}: Curve A, 3.2×10^{18}; Curve B, 1.8×10^{18}. Curve C, 2.8×10^{18}; Curve D, 4.8×10^{18}. Curve A shows nearly pure lattice response with peaks at $270cm^{-}1$ and $370cm^{-1}$ from the GaAs-like and AlAs-like TO modes, respectively. Curves B,C, and D show increased low wave-number reflectance, and plasmon-phonon minima related to free carriers.[31]

2.2 Measurement methods

A standard technique for visible light spectroscopy is to use a black-body source with a dispersive grating spectrometer as the wavelength selector. Infrared gratings are inexpensive and easy to make, especially at longer wavelengths, so grating spectroscopy should be an obvious choice for the infrared as well. But the infrared power available from a black body is small, especially at the very long wavelengths useful to characterize impurities, lattice modes, and free carriers. Grating spectroscopy does not make the

most effective use of the limited infrared power, although it gives good results when used with care. Instead, the dominant method is FTIR spectroscopy, whose more efficient use of the available power makes it preeminent.

Fourier spectroscopy also uses a blackbody source, but replaces the dispersive grating spectrometer with a Michelson interferometer. This gives the Fourier transform of the desired spectrum, known as the 'interferogram'. The interferogram requires extensive computer manipulation to yield the desired intensity versus wave-number spectrum, but the Fourier method gives a much higher signal-to-noise ratio than does grating spectroscopy. One reason is the Fellgett advantage, which states that the signal-to-noise ratio is higher when many wavelengths are measured simultaneously, as in Fourier spectroscopy, than when one wavelength is measured at a time, as in dispersive spectroscopy. The second reason is the Jacquinot or throughput advantage, which means that high resolution can be attained in FTIR spectroscopy without using narrow slits, whereas in conventional spectroscopy there is always a trade-off between resolution and the amount of light reaching the sample.

The basic process in FTIR spectroscopy is light wave interference. In the Michelson interferometer, radiation leaves the source and reaches the beam splitter. Part of the beam passes through the beam splitter and is reflected from a fixed mirror M1, whereas another part is reflected from the beam splitter and then from mirror M2, which is movable. As M2 moves, it changes the difference in length Δ between the paths the two light beams traverse. When the beams recombine they produce an intensity which depends on Δ, called the 'interferogram' $I(\Delta)$. Except for a constant multiplicative

factor, the interferogram is given by:

$$I(\Delta) = \int_{-\infty}^{\infty} S(f)[1 + \cos(2\pi f \Delta)]df = \frac{1}{2}I(0) + \int_{-\infty}^{\infty} S(f)\cos(2\pi f \Delta)df \qquad (2.46)$$

where $S(f)$ is the intensity spectrum of the source, f is the optical frequency in wavenumbers, and $I(0)$ is the intensity at zero path difference. The integral in Eq. 2.46 is the cosine Fourier transform:

$$S(f) = \int_{-\infty}^{\infty} [I(\Delta) - \frac{1}{2}I(0)]cos(2\pi f \Delta)d\Delta \qquad (2.47)$$

This is implemented by measuring the interference signal $I(\Delta)$ with a detector, whose output is then processed by a computer. All commercial Fourier systems include a computer with software to carry out the Fourier integral.

To measure sample transmission rather than the source spectrum, the sample is placed as shown in Fig 2.3. Then equation 2.47 yields $T(f)S(f)$ where $T(f)$ is the wavenumber-dependent transmission coefficient. If $T(f)S(f)$ is measured with the sample in place, and the source spectrum $S(f)$ is measured with the sample removed, the ratio of the two quantities gives $T(f)$ alone. A similar method, with radiation reflected from the sample instead of passing through it, yields the reflection coefficient $R(f)$,except that the reflected intensity is measured in relation to a 100be a piece of polished metal.

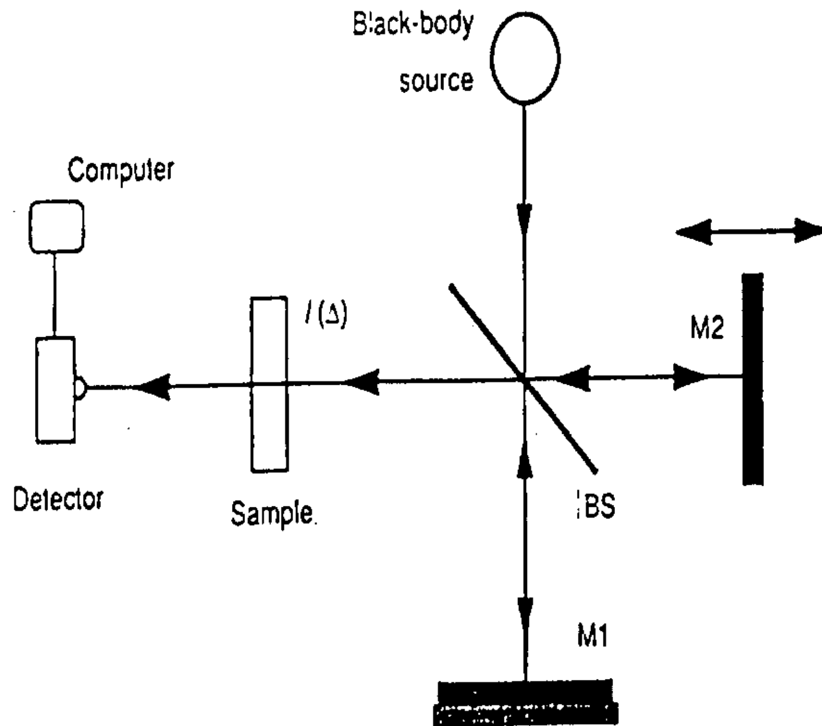

Figure 2.3: Michelson interferometer for transmissive FTIR spectroscopy. The black body illuminates the beam splitter (BS). The two resulting beams recombine in the interferogram signal $I(\Delta)$, where Δ is the difference in path length, which continues through the sample and to a detector. The computer performs a Fourier transform to recover intensity versus wavenumber. Reflectance can also be measured with a different geometry.

3 Positron annihilation spectroscopy

In recent years, positron annihilation spectroscopy (PAS) has been used increasingly as a sensitive probe to low concentrations of open-volume defects sites, such as Si dangling-bond sites. The PAS method is based on

1. the availability of beams of slow positrons that can be implanted at various controlled depths [32] in the order of a few micron range that is relevant to devices,

2. the propensity for positrons to seek out low density regions of a solid such as voids and vacancies [33][34],
3. the annihilation of positrons and electrons into γ rays that carry information about the local electronic environment and can escape through a semiconductor wafer without significant attenuation [35],

The PAS technique does not impose any restriction on the conductivity of the semiconductor material, nor does it require any special preparation, as do the standard techniques such as capacitance-voltage, deep level transient spectroscopy, and electron paramagnetic resonance. In the following section, we will describe the major components of a positron beam and theory of PAS.

3.1 Positron beams system

Positron sources

The most common techniques for the production of low-energy positrons are pair product in a high-energy accelerator or radioactive decay of a nucleus [36]. The first technique relies on high-energy electrons. When energetic electrons are decelerated in matter, photons are emitted through the Bremsstrahlung process. When the photon energy is more than twice the electron rest mass energy, positrons are produced by the pair conversion of these photons. This technique was used effectively at several laboratories. The advantage of an accelerator-based beam is that it can easily produce a pulse for depth-resolved measurements of positron lifetime. For the radioactive-decay technique,

the most commonly used radio-isotopes are Cu, Co and Na.

Moderators

Radioactive decay produces positrons over a wide range of energy with the distribution having the shape of the usual β-decay spectrum with a characteristic endpoint energy. Pair production by Bremsstrahlung photons also produces positrons with a wide energy-spread. To produce a monochromatic positron beam from such a broad energy spectrum, a technique known as moderation was developed. Moderation is achieved by using an annealed crystalline material, placed in front of and /or around the radioactive source. A suitable moderator material has a negative positron work function (ϕ_+), defined as the minimum energy required to take a positron from a point inside the material to the vacuum outside. The positron work function is negative for some materials, in which case the positrons that reach the surface after complete thermalization in the bulk will be emitted into the vacuum. The result is the emission of a monoenergetic low-energy positron beam with an energy distribution having a maximum energy of longitudinal motion ϕ_+ [37] and a spread in the energy of transverse motion characteristic of the multiple-scattering process that produced the thermalization in the bulk material.

Accelerator and transport system

The moderated positrons are usually extracted and transported to the target through a guiding magnetic field. The extracted positrons also contain unmoderated high-energy

positrons, and to avoid transporting them to the target, the source and target usually are not positioned along the same beam axis. The moderated positrons are usually drifted through an $\mathbf{E}\times\ \mathbf{B}$ filter to the axis containing the target, while the unmoderated positrons, which undergo only small changes in direction and, hence, are not brought to the same axis, are captured in a thick absorbing material. The filtered positrons then are accelerated to the desired energy. The positron beam can be inspected visually with a channel electrón multiplier array coupled with a phosphor screen.

Progress in computational methods for low-energy charged particle optics has accelerated the development of several positron beams that use electrostatic elements instead of magnetic elements [38]; electrostatic elements provide better control over the parameters of the final beam than the latter. In particular, micro-beams, which are suited for studying samples with a small cross-sectional area, have become feasible. The development of micro-beams was accelerated by the realization that successive stages of moderation can be used to enhance the "brightness" of the beam [39]. With such enhancement, the inherent limits set by the phase-space conservation and the original positron-emitting area (which is mainly due to the active area of the radioactive source) on the characteristics of the final beam can be overcome. In this scheme, moderated positrons from each stage are accelerated and focused onto the next moderator until the desired beam emittance is achieved. Because multiple scattering in the moderator material is not restricted by Liouville's theorem, and because the positron's diffusion length in the moderator material is about 200nm, the positron emitting area is reduced at each stage of moderation at the expense of a reduced (typically by a factor of 0.5) beam intensity. As more intense

positron sources become available, several stages of moderation have become practical, and beam spots with a diameter of few μm can be achieved.

3.2 Theory of PAS

A low-energy positron beam of tunable energy can provide a depth-resolved signal from the near-surface region of a solid. A quantitative interpretation of the depth-resolved signal requires a good understanding of the incident-energy-dependent positron implantation profile, eg,. the probability distribution $P(z;E)$, where $P(z;E)dz$ is the probability that a positron, incident with energy E, will be slowed to thermal energies between depth z,z+dz. Positron beams are generally used to study the distribution of defects in the top few μm of a solid material; for most materials, this will correspond to incident positron energies of $\leq 50keV$.

For such incident energies, positron-stopping profiles can be estimated by means of Monte-Carlo simulation. The resulting implantation profile for a homogeneous, semi-infinite target can often be approximated with reasonable accuracy by a Makhovian distribution [40]:

$$P(z) = \frac{mz^{m-1}}{Z_0^m} exp[-(\frac{z}{z_0})^m], \tag{2.48}$$

where z denotes the depth into the solid from the surface , m is known as a shape parameter, and z_0 depends on the incident positron energy and is related to the mean implantation depth, z, by

$$z_0 = \frac{z}{\Gamma(\frac{1}{m}+1)} \tag{2.49}$$

where Γ is the gamma function. For most studies involing Si and $Si - SiO_2$, $m \simeq 2.0$

is adequate. Then, the Makhovian distribution becomes a simple Gaussian-derivative profile. In many cases, including Si and $Si - Si0_2$, the mean depth, z in $\AA$, is related to the incident positron energy through a power law

$$z = \frac{A}{\rho} E^n, \tag{2.50}$$

where $E[keV]$ is the positron energy and $\rho[gm/cm^3]$ is the mass density. The parameters A and n are empirically found. For Si based systems, n=1.6 and A=4.0 $\mu gcm^{-2}keV^{-n}$. Thus, by an appropriate choice of beam energy, the mean depth can be varied between 1 nm and few μm.

After the positrons have been implanted, i.e., slowed down to thermal energies, they can still propagate some distance through the sample before they are annihilated; this must be accounted for when considering trapping of positrons by defects, especially when depth profiling of defect concentrations is needed. Often, this propagation can be described as diffusion in a medium containing a distribution of trapping centers, with appropriate boundary conditions imposed at internal interfaces and the free surface. In interpreting experiments where one is profiling the defect density on a scale that is large compared with the scattering mean-free-path of the positron, it is a reasonable approximation to treat the thermalized positron motion as a one-dimensional diffusion problem. Then, the time-dependence of the positron probability density $n(z)$, where $n(z)dz$ is the probability of finding the positron in a slice of thickness dz at depth z, is given by

$$\frac{\partial n}{\partial t} = D_+ \frac{\partial^2 n}{\partial z^2} - \frac{D_+ e}{kT} \frac{\partial}{\partial z}[E(z)n(z)] - \frac{n(z)}{\tau_{eff}} + n_0(z), \tag{2.51}$$

where D_+ is the positron diffusion coefficient, T the temperature, E the electric field,

e the positron charge, $n_0(z)$ the rate at which thermalized positrons are deposited at depth z, and $\tau_{eff}^{-1} = \tau_{bulk}^{-1} + \mu C_d$ is the probability per second that a given positron will be removed from the freely diffusing state, either by annihilation at a rate τ_{bulk}^{-1} or by being trapped at a lattice defect at a rate μC_d, where C_d is the defect concentration and μ the specific trapping rate. It is usually assumed that the rate of positron deposition is sufficiently high to treat the problem as one of steady state, $\partial n/\partial t = 0$, so that a solution is required to the ordinary linear second-order differential equation.

$$\frac{d^2n(z)}{dz^2} - \frac{d}{dz}[\frac{n(z)}{\Lambda(z)}] - \frac{n(z)}{L^2} + \frac{n_0(z)}{D_+} = 0 \tag{2.52}$$

where $L = (D_+\tau_{eff})^{1/2}$ is the positron diffusion length and $\Lambda = kT/Ee$ is a parameter with the dimension of length which characterizes the electric field $E(z)$.

Positrons participating in the annihilation process are predominantly thermalized. Therefore the relative motion of the electron-positron pair will be dominated by the electron motion, and the Doppler shift will be a suitable signature of the electronic environment around the annihilation site. For nonrelativistic electrons, the Doppler shift of the annihilation γ ray is given by

$$\partial E = cp_l/2, \tag{2.53}$$

where p_l is the component of the pair momentum along the γ-ray emission. For a typical electron energy of a few eV and a thermlized positron we get $\partial E \simeq 1.2keV$. In an experiment where energies of several annihilation photons are recorded, the Doppler shift of the individual $gamma$-ray line will contribute to an overall broadening of the annihilation photopeak; this is often called Doppler broadening.

Although, in principle, the annihilation photopeak can be deconvoluted to extract the electron momentum distribution, a simple shape parameter is commonly used to characterize the photopeak. Two parameters, S (for shape) and W (for wings), are usually employed. The definitions of these parameters are schematically illustrated in Fig 2.4. The S parameter is defined as the ratio of the counts in a central region of the spectral peak to the total counts in the peak, and W is defined as the ratio of counts in the wing region of the peak to the total counts in the peak. The S and W parameter is related to the shape of the one-dimensional momentum distribution:

$$S, W = \sum_{1} \int_{-\infty}^{\infty} \int_{-\infty}^{\infty} dp_x dp_y \rho(p) \backslash \sum_{tot} \int_{-\infty}^{\infty} \int_{-\infty}^{\infty} dp_x dp_y \rho(p) \qquad (2.54)$$

where $\sum_1$ is over the appropriate energy window for S and W definition, $\sum_{tot}$ is over the full annihilation photopeak, $\rho(p)$ is the momentum distribution of the annihilating electron-positron pair, p denote the momentum of the electron positron pair and p_z is along the direction of emission of the detected photon.

The S or W parameter has a simple relationship to the Doppler broadening; for example, if the annihilation peak is narrow, which results when positrons annihilate predominantly with slow-moving electrons, the S parameter is large, and vice versa. Thus annihilations with valence electrons are reflected in S parameter and those with core electrons in W parameter. More often, S and W parameters show opposite behavior.

The use of simple parameters such as S and W yield extensive information about open-volume-type defects and internal electric fields. The absolute values of S and W parameters have little physical relevance, since they are essentially decided by the posi-

tion of the windows chosen in their definition. It is the relative change in these parameters that carries information about the annihilation sites. Therefore, the S and W parameters are usually normalized to a reference value corresponding to the defect-free value of the material under investigation. The normalized values then can be compared between different samples and different experimental arrangements. Because the Doppler broadening parameters can be measured very rapidly, they are used more extensively in defect related studies.

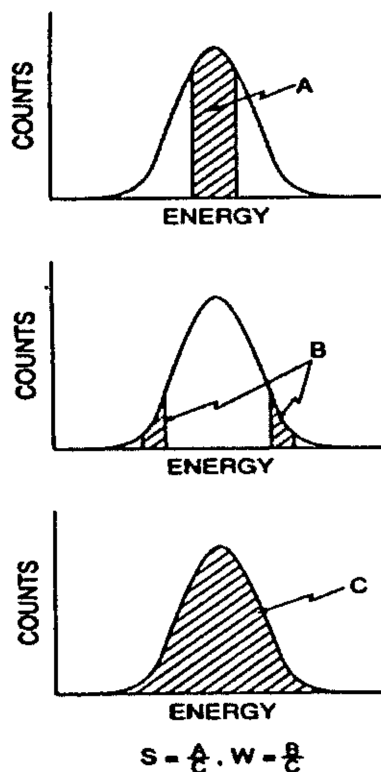

Figure 2.4: Definition of S and W parameters. The measured annihilation peak contains broadening caused by Doppler shift and instrumental resolution. A typical value for the windows are : for region A from 510.2 to 511.8 keV, for region B from 507.8 to 509.3 and from 512.7 keV to 514.8 keV, and for region C from 506to 516 keV

Chapter 3

Metastability in Hydrogenated Amorphous Silicon

Metastability in electronic materials is typically characterized by two factors, one is the electronic quality and the other is the structural stability. Electronic quality is a relative measure for the efficiency with which a material can be excited out of its ground state, Q, into an excited state, Q^*. Different techniquies can be used to excite the material such as irradiation with photons, by charge carrier injection, or by application of an external field. Structural stability describes how the bonding configurations of the same material may change under conditions of prolonged or repeated excitation generally encountered in all electronic devices during operation. The qualitative difference between a stable and an unstable material can be visualized in terms of the energy-configuration diagrams in Fig 3.1. Metastable structures are characterized by energy minima for Q and Q^* that occur at sufficiently different configurations. Electronic excitation is then followed by a significant lattice rearrangement as the system relaxes into the new structure corresponding to the minimum of the Q^* curve. If this minimum is lower in energy than the crossing point of

the Q and Q^* curves, the relaxed excited state is metastable in the sense that the system has to overcome an energy barrier, E_B in order to return to the ground state.

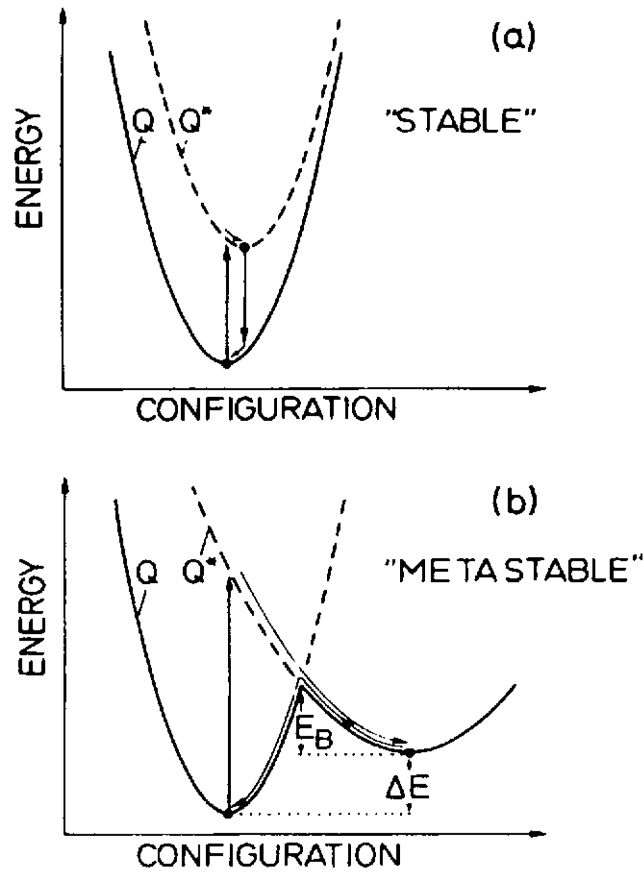

Figure 3.1: Energy-configuration diagrams for stable (a) and metastable structural configurations (b). Q and Q^* denote the ground state and excited states of the system, respectively.

There are three principal components that will favor the formation of metastable configurations in a material :

1. Long lifetimes of electronically excited states.
2. Sufficient localization of the electronic wavefunctions.
3. Relatively weak binding potentials for constituent atoms.

In particular, hydrogenated amorphous silicon can be expected to be quite susceptible to the formation of metastable structures, because it generally meets the three criteria discussed above. The bonding disorder inherent in the amorphous phase gives rise to both a large densities of localized electronic levels such as tails of valence and conduction band. A large number of pre-strained structural units with low force constants for atomic displacements, e.g., weak or wrong bonds. Preparation of low density of deep-levels defect density of *a-Si:H* is similar to that of crystalline compound semiconductors that allow a high level of electronic excitation under illumination or external bias. Experimentally, metastable structural behavior has been observed in *a-Si:H* such as light induced reversible degradation and thermal equilibration effect. In the following section, we will discuss these phenomena.

1 Staebler-Wronski Effect

Light induced degradation in *a-Si:H* was first observed by Staebler and Wronski in 1977 [41]. By extended illumination with visible light of *a-Si:H*, a decrease in photoconduc-

tivity and dark conductivity is produced, though the extent of the decrease depends on the initial defect density and doping level of the sample. At this degraded state, the conductivity is essentially stable at room temperature and can be reversed by annealing at 150 °C. It has subsequently been found that the Staebler-Wronski effect can also produce by irradiation with ions [42], electrons [43] and X-rays [44]. It is presently believed that the recombination of the irradiation-produced excess electron-hole pairs breaks the weak *Si-Si* bond. This results in the generation of dangling bonds. These defects act as recombination centers, decreasing the photoconductivity, and move the Fermi level toward midgap, decreasing the dark conductivity. The light-induced effects are characterized by very slow creation and annihilation rates. It is reported that illumination with sunlight results in the creation of about 10^{17} cm^{-3} defects after many hours. The effective capture cross-section for the defect creation is estimated to be no more than 10^{-25} cm^2, assuming an electron trapping mechanism, which is ten orders of magnitude lower than normal capture cross-sections for an electronic state. Similarly, since the induced defects in *a-Si:H* are stable almost indefinitely at room temperature and are only annealed above 150 °C, the rate of annealing must be much slower than any normal excitation rate of electrons or holes to the band edge. The low creation and annealing rates strongly suggest that a structural change is taking place rather than a change in occupancy.

The irradiation-induced defects in *a-Si:H* remains an unsolved problem. The microscopic models developed to explain the formation of stable defects can be divided into two classes: (i) those that involve the motion of bonded hydrogen; and (ii) those that do not. For the first class, a weak *Si-Si* covalent bond is broken, when an electron-hole pair

recombine at this bond site, i.e. at a localized band tail state. Hydrogen motion has been involved in order to stabilize the broken covalent bond, that is , to prevent the two new dangling bonds from rejoining and reforming a covalent bond [45][46][47]. The second model postulates that a back bonded hydrogen could switch its position and thereby produce a dangling bond pair that is separated by a distance of at least 7Å, decoupling the two spins. Additional motion of hydrogen could conceivably further separate the dangling bond pairs [48][49].

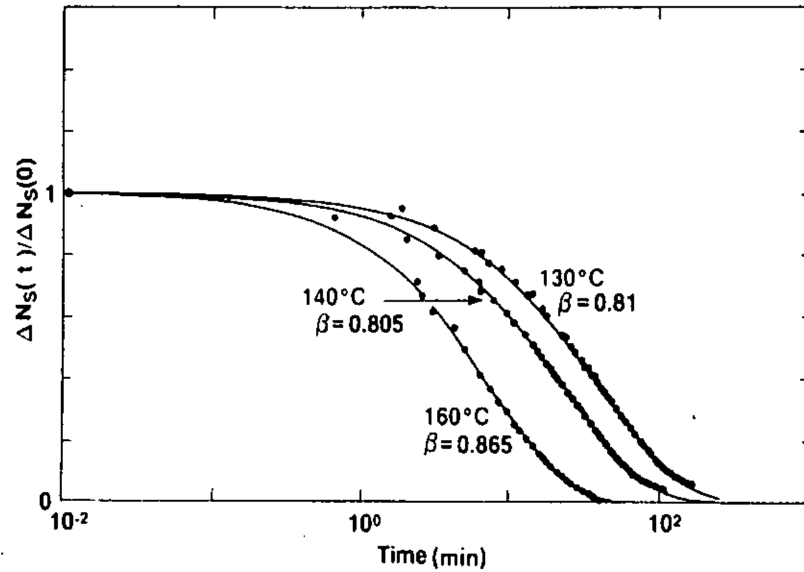

Figure 3.2: Time decay of normalized light induced spin density for various temperatures. The solid circles are the data points while the solid lines are fits to the data using a stretched exponential time dependence.[50]

Further support for the notion that hydrogen motion is directly involved in the stabilization of metastable defect creation is provided by comparing the dispersive hydrogen diffusion with the time dependence of the creation and annealing of the excess defects.

As illustrated in Fig 3.2, the annealing of light-induced defects determined by electron spin resonance measurements is shown. The defect density accurately follows a stretched exponential time dependence [50]:

$$\Delta N = \exp[-(t/\tau)^{\beta}] \tag{3.1}$$

where $0 < \beta < 1$.

The time to anneal away the excess spin density becomes shorter at higher anneal temperatures, while β also increases with temperature. The relation between the dispersive time dependence of hydrogen motion and the stretched exponential annealing of light-induced defects will be discussed in detail later on.

2 Thermally Induced Metastability in Amorphous Silicon

There is a growing interest in thermally induced defects in *a-Si:H*. Recent studies of doped *a-Si:H* have found that the background density of localized states such as electrically active dopants and dangling bond defects are metastable [51][52][53]. After the sample is annealed at above 150°C in the dark and then rapidly cooled, the dark conductivity of n-type and *a-Si:H* decreased by nearly a factor of two over a period of several weeks, while p-type material just needs several hours. As shown in Fig 3.3, the relaxation rate of the occupied bandtail density n_{BT} is a sensitive function of temperature, so that the time needed to reach the steady state value is shortened to a few minutes at 125 °C.

The density of electrons residing in band tail states is related to the densities of donors (N_{donor}) and dangling bonds (N_{DB}) by the expression:

$$n_{BT} = N_{donor} - N_{DB} \tag{3.2}$$

When the samples are annealed above an equilibration temperature T_E the original band tail density is restored. T_E is near 80 ^{0}C for p-type *a-Si:H*, 130 °C for n-type doped material and is $\sim$ 210 ^{0}C for undoped *a-Si:H*.

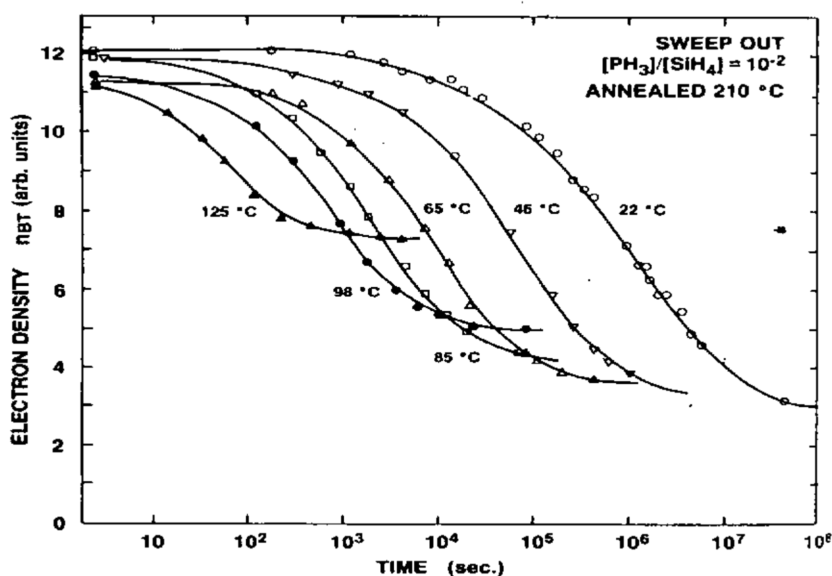

Figure 3.3: Time decay of the occupied band tail density n_{BT}, measured by the voltage pulse charge sweep-out technique, for various temperatures.

Previous studies showed that the time for the density of localized states to reach equilibrium is thermally activated, becoming longer at lower temperatures. The equilibration times have an activation energy of $E_T \sim 0.95$ eV and a pre-exponential factor of approx-

imately $\tau_0 \sim 10^{-10}$ for n-type *a-Si:H* and $\tau_0 \sim 10^{-11}$ for p-type doping. A consequence of the thermally activated equilibration rate is that the electronic properties are very sensitive to the rate at which the sample is cooled following a high temperature anneal. That is, if the sample is cooled more rapidly from above T_E than the equilibrating defect structure can follow, then a density of states representative of the high annealing temperature will be quenched or frozen in at room temperature. Cooling at a slower rate allows the changing defect structure to remain in equilibrium down to lower temperatures. The material will depart from equilibrium when the time to reach equilibrium is longer than the cooling rate. The electronic properties exhibit a slow, stretched exponential relaxation below T_E, as the defect structure slowly relaxes back to its equilibrium configuration.

3 Stretched exponential relaxation

Stretched exponential relaxation is a fascinating phenomenon because it describes the equilibration of a very wide class of disordered materials. The form was first observed by Kohlrausch in 1847, in the time dependent decay of the electric charge stored on a glass surface, which is caused by the dielectric relaxation of the glass. The same decay is observed below the glass transition temperature of many oxide and polymeric glasses, as well as spin glasses and other disordered systems.

The bonding disorder of a glass suggests that a decay with a single time constant is not expected, but instead an average over the structural configuration. One possibility is a local variation in decay rates described by a distribution of time constants $F(\tau)$, so

that

$$n(t) = \int F(\tau) \exp(-t/\tau) d\tau \tag{3.3}$$

The integral in Eq. 3.3 contains the implicit assumption that the relaxation events occur independently at each site. An alternative model describes the relaxation in terms of a hierarchy of processes, in which increasingly large configurations of atoms are involved in the relaxation as time progresses. The relaxation processes are then no longer independent of each other, but evolve with time. These alternative descriptions of the relaxation are simply expressed by rate equations of the form,

$$dN/dt = -k(x)N \tag{3.4}$$

and

$$dN/dt = -k(t)N \tag{3.5}$$

In the first case, the spatial distribution of rate constants leads to Eq. 3.3. The time dependence of $k(t)$ in the second case reflects a relaxation which occurs within an environment that is itself time-dependent. If k has a time dependence of the form,

$$k(t) = k_0 t^{\beta-1} \tag{3.6}$$

then the integration of Eq. 3.5 gives

$$N(t) = N_0 \exp[-(t/\tau)^{\beta}] \tag{3.7}$$

Chapter 4

Experiment

1 $1/f$ noise measurement

In studying the flicker noise of the tested device, the background noise such as shot noise and Johnson noise, as well as noise in the biasing circuit and the amplifier have to be eliminated or the frequency range and biasing conditions must be chose such that $1/f$ noise dominates over other noise sources. We measured the excess noise power over a wide range of frequency, in which flicker noise dominate. Sources of the background noise include:

1. Johnson noise originated from thermal fluctuations in the electron density within the device. These fluctuations give rise to an open-circuit noise voltage :

$$V_{noise}(rms) = (4k_BTR\Delta f)^{1/2} \tag{4.1}$$

where k=Boltzmann's constant (1.38×10^{-23} J/K), T is the temperature in Kelvin, R is the resistance in ohms, and Δf is the bandwidth of the measurement in Hz.

This type of noise is typically two or three orders of magnitude weaker than device noise at low frequencies.

2. Shot noise originated from the fact that an electric current flow is the flow of discrete electric charges, not a smooth fluid -like flow. The finiteness of the charge quanta results in statistical fluctuations of the current. The shot noise or current noise, is given by:

$$I_{noise}(rms) = (2qI\Delta f)^{1/2} \tag{4.2}$$

where q is the electron charge (1.6×10^{-19} Coulomb), I is the RMS AC current or DC current depending upon the circuit, and Δf is the bandwidth. This type of noise is significant at high d.c. current. For our case the biasing current was typically set at $7\mu A$ to $18\mu A$ and shot noise was negligible compared to the resulting flicker noise.

3. Currents flowing through the ground connections can give rise to noise voltages. This is especially a problem with signal frequency ground currents. Cures for ground loop problems include:

    - Grounding everything to the same physical point.
    - Using a heavy ground bus to reduce the resistance of ground connections.
    - Removing sources of large ground currents from the ground bus used for small signals.

Before measurement, the background noise was measured by applying a zero bias to the device. Make sure that the background noise must be at least one order of magnitude

smaller than the device noise.

1.1 Experimental setup

The experimental setup for the noise measurement is shown in Fig 4.1, the sample was placed on a copper block inside a nitrogen purged chamber. Resistive heaters in the Cu block allow the sample temperature to be varied from room temperature to 450 K. The temperature was monitored using a silicon diode sensor sitting next to the sample. The temperature was controlled by a LakeShore DRC-91C temperature controller. In the experiment, the sample was fabricated in four probe configuration. A constant current was supplied across one pair of electrodes using a Kiethley 220 constant current source. Voltage across the other pair of electrodes was amplified using a battery-operated low noise voltage pre-amplifier PAR-113 which has a maximum gain of 10^4 and a maximum upper roll-off frequency of 300 kHz. The signal from the amplifier was then sent to the HP3561A spectrum analyzer, which perform a real-time fast Fourier transform (FFT) on a 1024-point time buffer. The voltage power spectra were then averaged typically 1000 times for accuracy. The noise spectra were stored in the spectrum analyzer and then transferred to computer for analysis. In order to eliminate the extraneous noise, the sample and the amplifier are enclosed in a metal screen box, which are in a shield room.

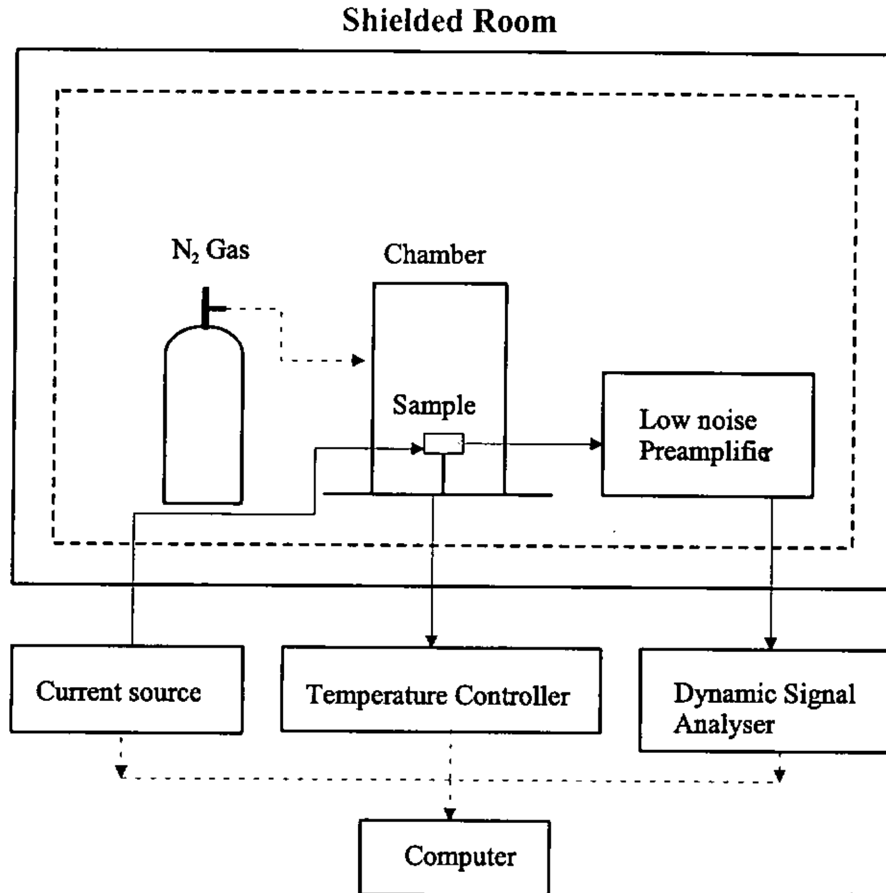

Figure 4.1: The experimental setup for low frequency noise measurement.

1.2 Sample preparation

The films used in these studies are n-doped *a-Si:H* deposited by PECVD in a three chambers system, grown at Institute of Semiconductor, Chinese Academy of Sciences. The gas phase doping level was 3×10^{-2} PH_3/SiH_4. The rf power was 0.05 W/cm^2 (13.56 MHz), yielding a deposition rate of ~0.8 Å/s. The film was deposited onto 7059 corning glass substrates. The substrate temperature was 230 ^0C. The thickness of the

films are approximately 1 μm thick.

The electrical contact on the *a-Si:H* was fabricated in four-probe configuration which is shown in Fig 4.3. This configuration was chosen because the noise from the contact resistance between *a-Si:H* and metal contact can be eliminated. The sample was first cut into 0.9 mm $\times$ 0.9 mm. It was then cleaned with a standard cleaning procedure. Positive photo-resist was spin on the films. The sample was then soft baked at 80 ^0C for 20 min to dry the organic solvent such that the positive photo-resist can strike on the films. The film was exposed to UV-light for 30 second with a covering mask. It was then immersed in the developer to develop the pattern on the photoresist. The coplanar electrode was made of evaporating a 1000 ÅCr layer. The film was then placed in an ultrasonic cleaner which was filled with acetone for lift-off process. The metal contact and the *a-Si:H* film was scratched by a diamond scriber in order to achieve the four-probe configuration.

Before measurement, the film was annealed at 450K for 30 min to removed light induced metastable effect and any surface effect. The cooling rate to cool the film from high temperature to room temperature is very important because as mentioned in previous section, the electronic state of the film is very sensitive to the cooling rate. So we have to control the cooling rate, such that the result is comparable. The annealing of the sample was placed in the chamber as mentioned before. The cooling rate of the film was controlled by temperature a controller which was programmed by using LabView.

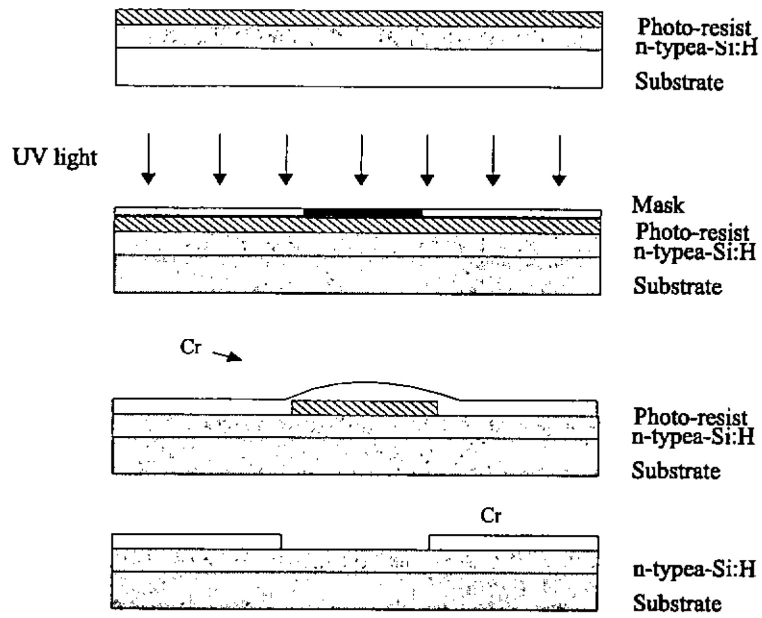

Figure 4.2: fabrication procedure for the Cr contact.

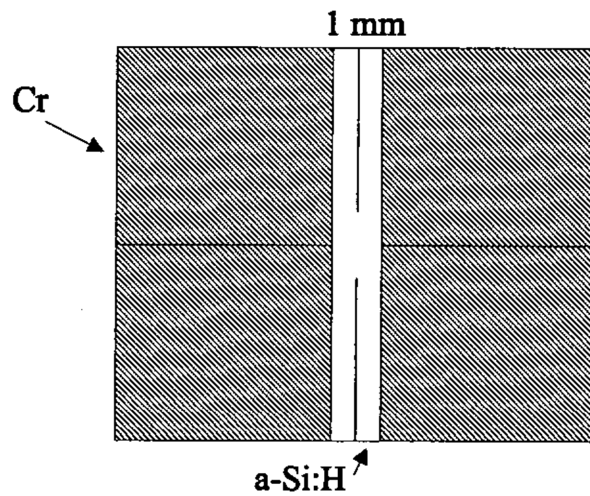

Figure 4.3: Coplanar electrode configurations used to measure noise frequency noise and conductance.

2 Positron beam system

The positron beam employed in this work is the positron beam facility of the University of Hong Kong which is magnetically guided beam of intensity about 1×10^5 per second and with a beam diameter of 6-7mm. A general schematic view of the beam is given in Fig 4.4, from which it can be seen that the beam can be divided into three main parts, the positron gun in which the low energy flux of positrons originates and the $E \times B$ filter section. The positron gun chamber is shown in more detail in Fig 4.5 and comprises of two parts, the positron gun in which the low energy flus of positrons originates and the $E \times B$ filter section. The latter was not used in the present studies, because the fast positron and gamma ray backgrounds were not sufficient to significantly distort the spectra. The filter and the positron gun are both housed in a long cylindrical vacuum tank of 250mm diameter. Surrounding the vacuum tank and accurately aligned with it are 7 equally separated 1m diameter quasi-Helmholtz coils the purpose of which is to provide an approximately uniform axial magnetic field, while at the same time allowing heating coils to be placed around the tank for UHV baking.

More detail regarding the positron gun source can be seen from Fig 4.6. The primary source of positrons are two 15m$Ci^{22}Na\beta^+$ sources deposited on Pt tips, Pt being used because of its high Z for efficient β^+ backscattering and vacuum compatibility. The Pt tips are covered with a Ti foil so as to prevent the ^{22}Na microcrystal source from flaking off into the vacuum. The sources are positioned close to the W(110) back-reflecting single crystal moderator as shown in the insert of Fig.4.6. Positrons implanted into the

moderator are thermalized within 1ps and then undergo diffusion. A small fraction of positron that diffuse back to the surface of the moderator are able to be re-emitted from the surface as the positron work function of W is negative. Consequently, as also shown in the insert, a flux of low energy positrons is emitted into the vacuum thus forming the origin of the beam. Also seen from Fig 4.6 is the fact that the ^{22}Na sources are located on the end of Mo source plugs which themselves are imbedded in a large cylindrical block of antimonial lead (4be both harmful to personnel working on the beam and would cause unwanted signals in the gamma ray detector used at the target. Backward going gamma radiation is also blocked since the W(110) moderator is itself placed on a Mo plug.

The efficiency of the moderator decreases as the beam is operated for a long period of time, because of the accumulated radiation dose to the moderator and because oxide continuously builds up on the moderator surface. The beam intensity is regularly checked to make sure that the moderator efficiency is still high enough of useful beam operation, otherwise the moderator has to be re-annealed. The annealing is carried out by electron beam heating method. In order to enhance the heating efficiency, a heated W cathode is fixed behind the moderator and at the center of the Mo moderator supporter, causing most of the electrons to strike the rear of the moderator and produce a temperature as high as 2000°C in very short time. To accomplish this the moderator is withdrawn out of the lead block to the position M_1 as shown in Fig 4.5. Here by electron beam heating from behind the crystal W(110) is heated to 2200°C under UHV conditions. After it has been cooled sufficiently it is then returned to its active position inside the lead block. Also seen in Fig 4.6 is the extractor grid which is placed just in front of the radioactive

Pao Yue-Kong Library
PolyU • Hong Kong

sources, but not in contact with them. Separate electrical potentials can be applied to the moderator, the sources and the extractor grid, and by adjustment of these three potentials the beam flux can be maximized by optimization of the extraction.

After traversing at the low kinetic energy of 150eV a long section of evacuated pipe surrounded by a solenoid, the positrons strike the sample which is situated at the end of the beam within a target chamber. The target chamber used for the measurements of this work was a temporary structure based on a standard 5 way cross and is shown in Fig 4.6. The sample is held by clips onto a sample holder connected to a high voltage feedthrough. This enables the large negative high voltage to be placed on the sample. The positrons as they enter the target chamber suddenly experience a strong accelerating electric field causing them to be accelerated into the sample at an energy corresponding to the potential applied to the sample. The pressure in the experimental chamber is kept at about 1×10^{-9} Torr by the use of an ion pump. The "down beam" flange has a channel plate imager attached to it, which enables the positron beam lateral profile to be imaged on a phosphor screen in the event of the beam being lost. The imager is at intervals used to check that the position of the beam has not moved but otherwise it is not used. On the other side of the chamber a high purity Ge detector is positioned as close to the chamber as possible and this detector picks up the 511keV annihilation radiation from the sample from which the "S-parameter" is eventually obtained. On the side of the target chamber opposite the Ge detector is a view flange, which allows the user to check that the sample is in the correct position.

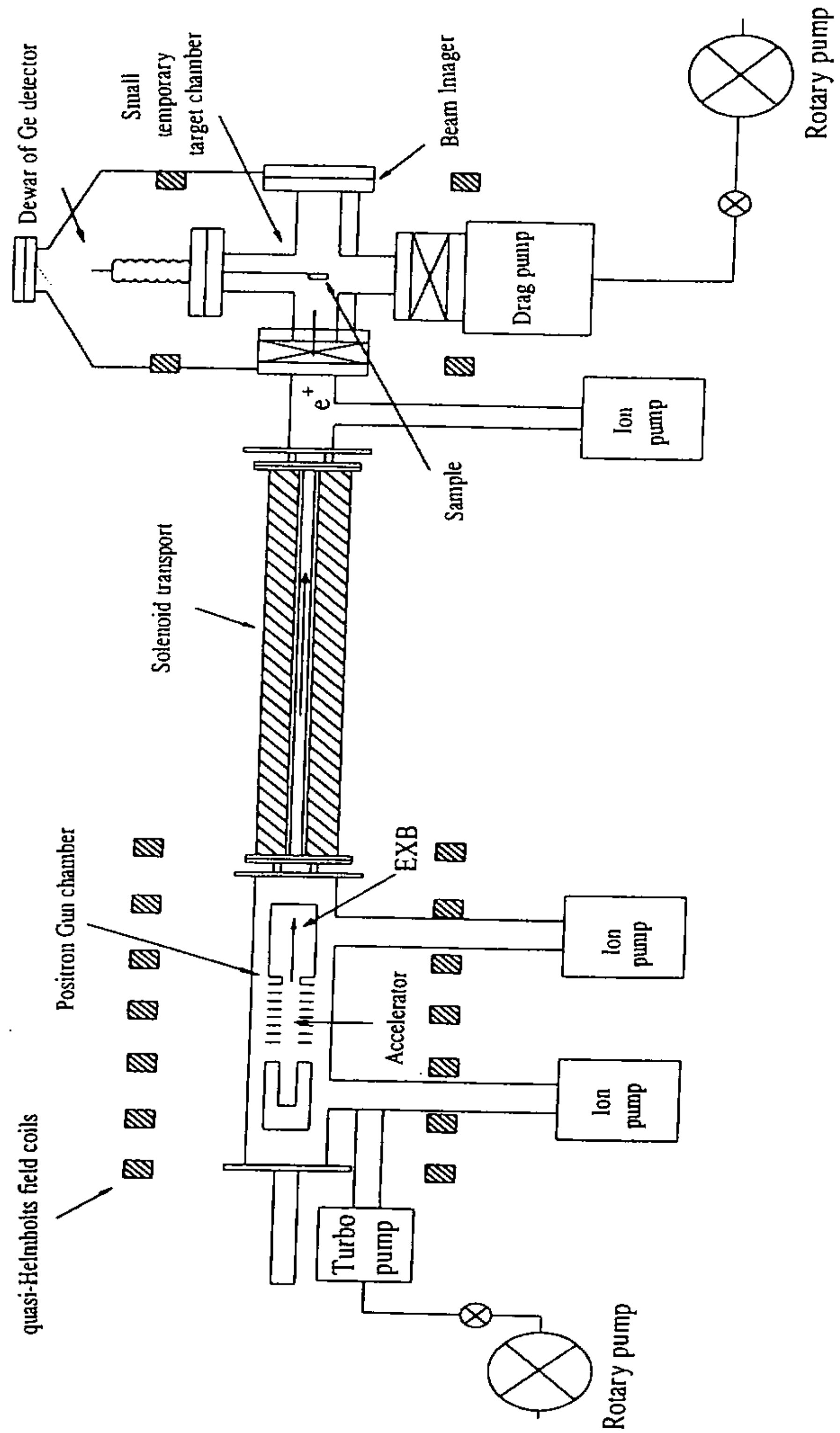

Figure 4.4: Magnetic transportation-general beam

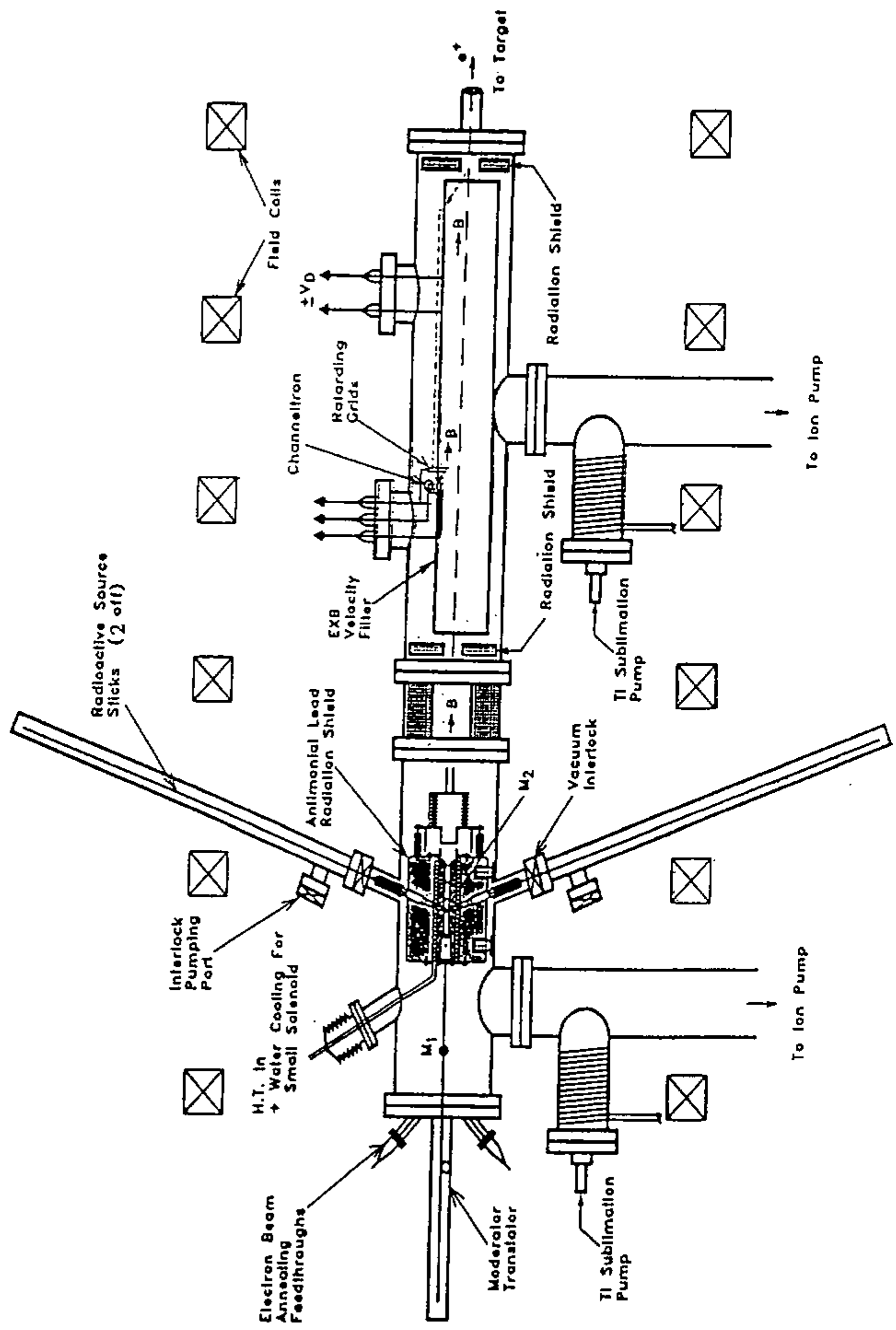

Figure 4.5: Positron Gun Chamber.

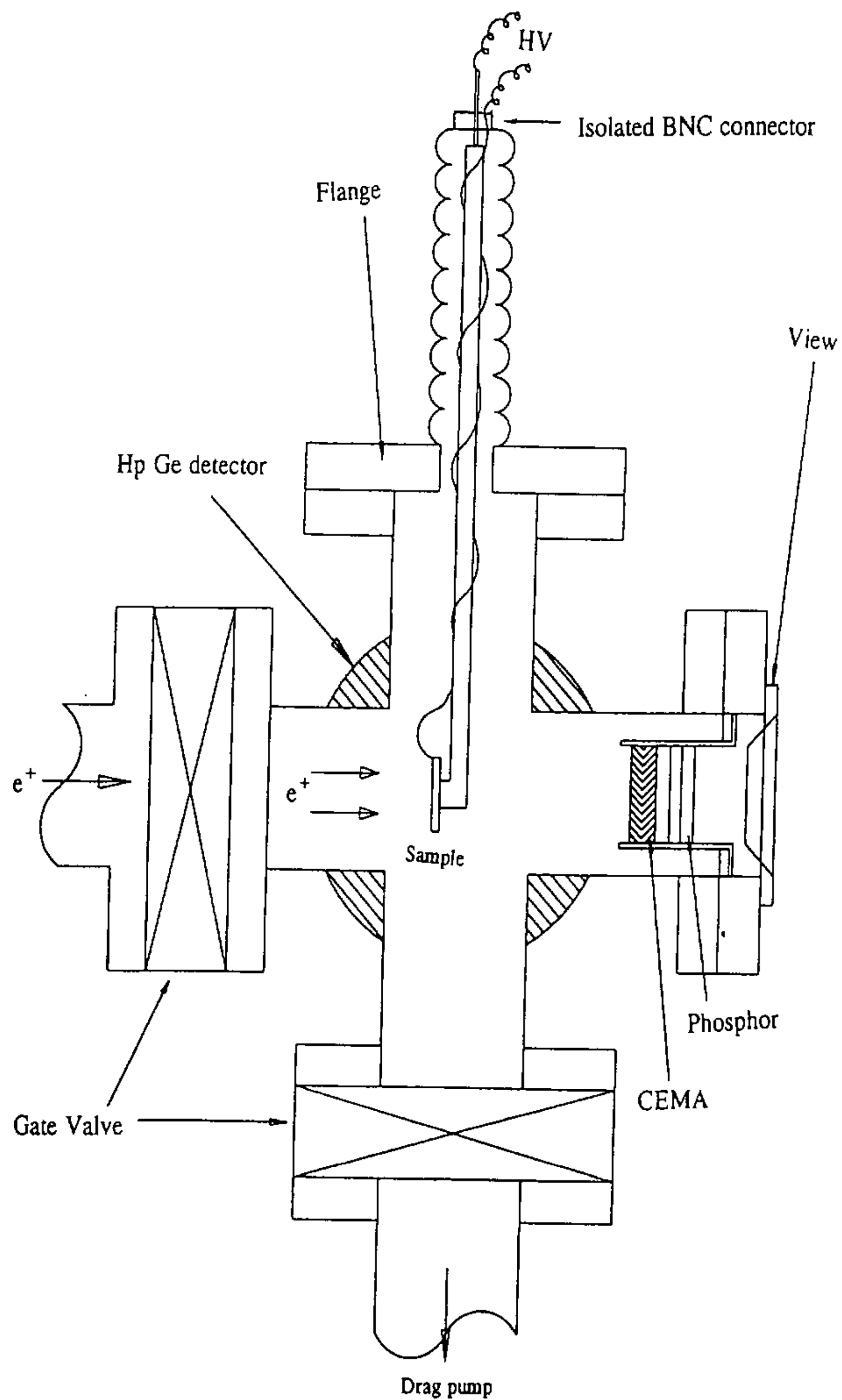

Figure 4.6: Source and moderator.

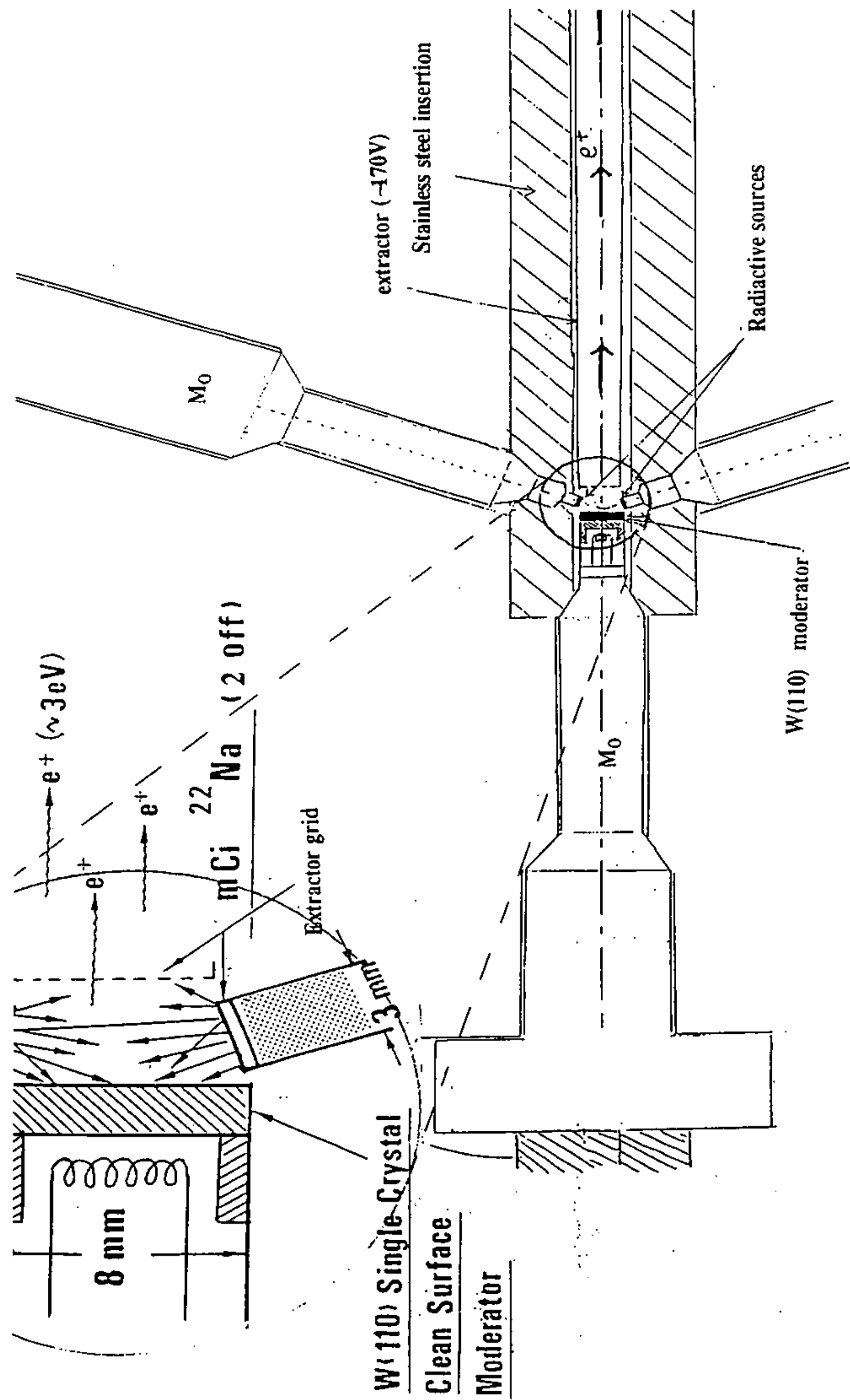

Figure 4.7: Temporary target chamber.

3 FTIR spectrometers

The FTIR spectrometer that we used is Perkin-Elmer 16PC spectrophotometer which is connected to a DEC 316SX computer. The optical system of the spectrometers contains a low power helium-neon laser which emits visible light at a wavelength of 633 nm. The power rating is less than 0.3 mW. The optical system and the sample holder of the system was shown in Fig 4.8 and 4.9. The sample was place on the crystal and covered was a pressure pad. The data range of the system is 7800 to 100 cm^-1.

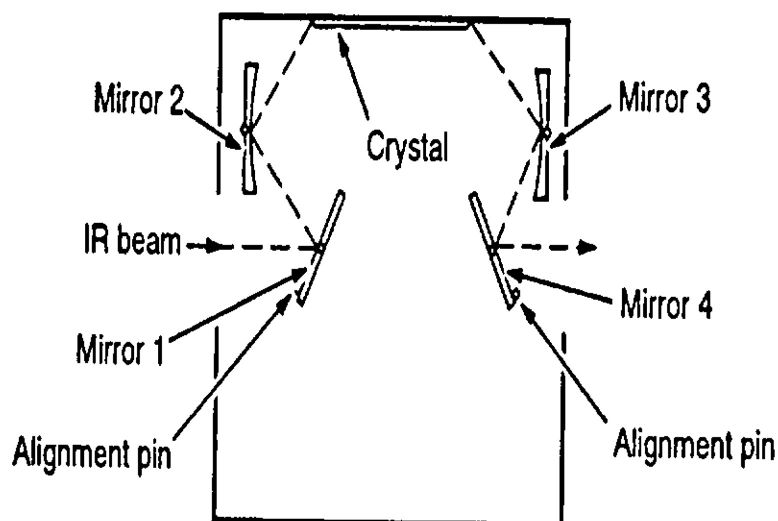

Figure 4.8: Optical Path of sample holder

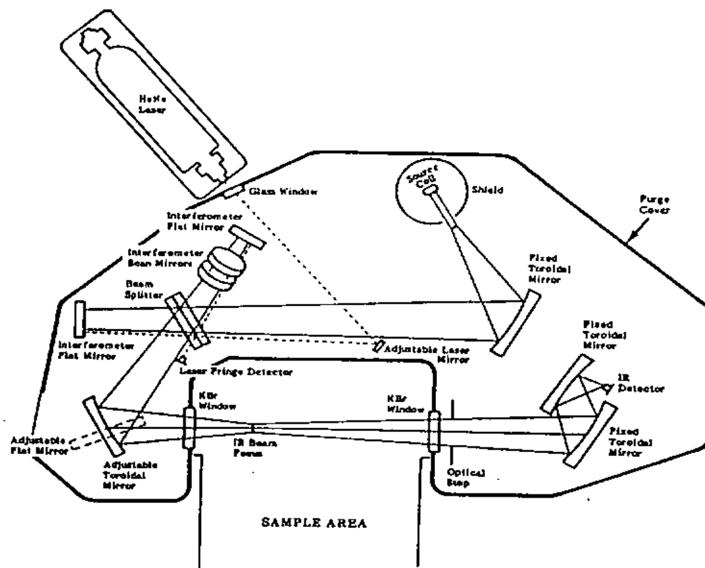

Figure 4.9: Model 16PC Optical System

4 Experiment I : Low-frequency noise of thermal equilibration effects in *a-Si:H*

Previous studies [50] have demonstrated that the density of electronically active dopants in n-type *a-Si:H* is governed by a metastable thermal equilibrium. When the cooling rate exceeds the rate at which the localized state distribution comes into equilibration, the system is frozen into a metastable non-equilibrium state. Thus noise can be used to characterize thermal equilibration. In order to study the noise measurement for the equilibration effect, the sample was annealed at 450 K and then cooled with different cooling rates.

To investigate flicker noise for thermal equilibration effect in n-type hydrogenated amorphous silicon resistive devices, the film was annealed at 450 K for 30 min. This annealing temperature was chosen because it is high enough for the hydrogen matrix to relax to the equilibrium configuration but does not affect the silicon network. It is then cooled to room temperature at a rate of 0.5 K/s. The voltage noise power spectra and the conductance of the device was characterized, using a four-point probe technique on a 1mm $\times$ 1mm resistive device, from room temperature to about 420 K with the device biased by a current source from ranging 7 μA to 15 μA. The experiment was repeated with the device annealed again and subsequently cooled at a rate of 0.02 K/s.

5 Experiment II : Low frequency noise and light induced Metastability

Light induced metastability is an important research area in *a-Si:H* materials. It is the main cause for device degradation in *a-Si:H* based solar cells and detectors. It is therefore important to characterize the effects on the material properties due to optical illumination. In this thesis, we report detailed examinations on photo-induced metastability through the characterization of the low-frequency noise, positron beam annihilation spectroscopy and Fourier transform infrared spectroscopy.

To investigate noise measurement due to light induced metastability, two light source were used. One is the ORIEL Instruments model 66011 lamp house with 500 W Xenon (Xe) lamp. The other light source was an Omnichrome Helium-Cadmium laser with a wavelength of 325 nm and a power of 10 mW at a beam diameter 1.2 mm. The setup was shown in Fig. 4.10. The light emitted from the Xe lamp filtered using the AM-0 and AM-1 filters to simulate one sun exposure. To avoid heating of the sample, the *a-Si:H* film was placed on a Peltier effect semiconductor thermoelectric device to keep the sample temperature at approximately 22 °C during light exposure. This avoid self-annealing of the film during exposure. In order to have a good cooling condition, the semiconductor thermoelectric devices was placed on a large heat sink with a cooling fan. The temperature was monitored by a type-K thermal couple sitting next to the sample. After the sample was exposed to light for 30 min to 1 hour, it was placed in a chamber for noise characterization as shown in Fig 4.1. Since the duration of the

noise experiment lasts over 30 hours, the time dependence of low-frequency noise and the device conductance were characterized with the device temperature carefully set at 300 K to avoid thermal fluctuation induced resistance change. To study light induced metastability using laser illumination, the sample was place in a chamber which has a sapphire window. The sample was exposed to HeCd laser at a wavelength of 325nm through the sapphire window. After each 15 min expose, the noise power spectra and the conductance was measured. The temperature was controlled by a Lakeshore 91C temperature controller. For $1/f$ noise measurement, the device was biased by constant current source from 7 μA to 15 μA and was measured after each 15 min exposure.

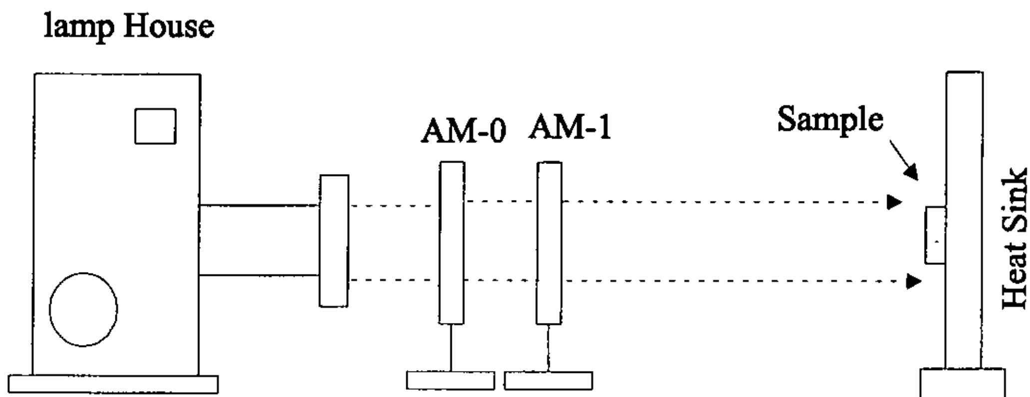

Figure 4.10: Experimental setup for light induced degradation.

Chapter 5

Experimental Results

In this Chapter, the experimental results on the 1/f noise measurements are presented. The experiments performed are categorized into three main areas :

1. DC conductivity,
2. Thermal equilibration effect,
3. Light induced metastability.

1 DC conductivity

The main experimental results involve fluctuations in the coplanar voltage in n-type *a-Si:H*. The device performance is concerned with the condition of the contacts. Details on the structure of the device and its contacts were provided in Section 4. The contacts were designed to provide an ohmic interface with the material so it is important to

verify this. As shown in Fig 5.1, the device display linear current-voltage characteristics from -4.5×10^{-5} to 4.5×10^{-5}A, passing linearly through the origin, consequently the fluctuations in the current imply changes in the bulk resistance of the *a-Si:H*, provided that contact effects are eliminated as a source of the noise.

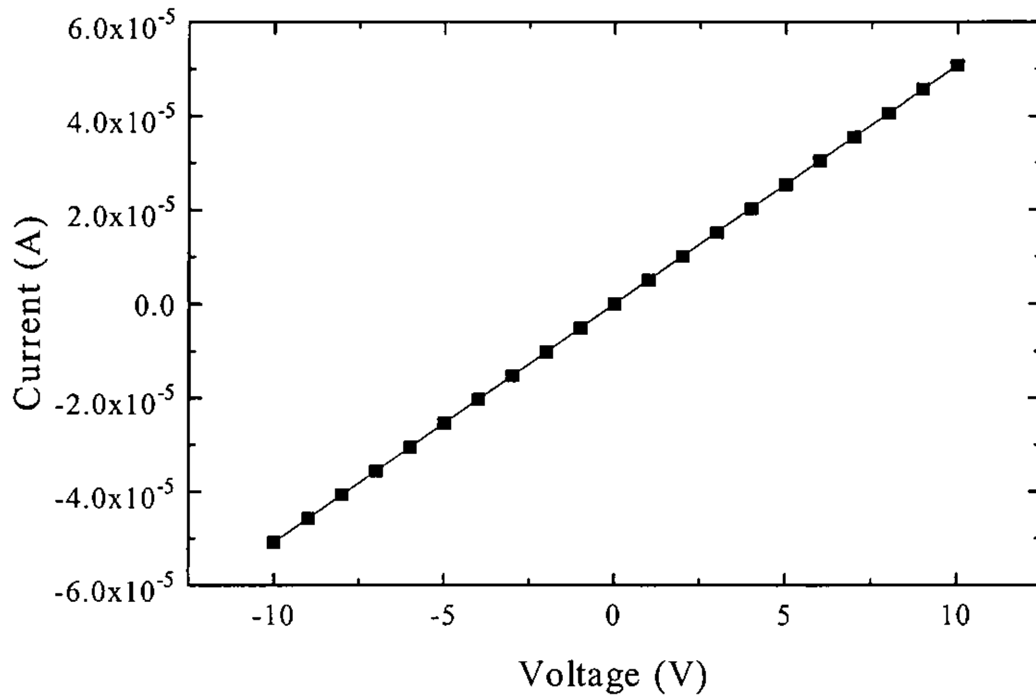

Figure 5.1: The I-V characteristics of the sample at room temperature.

Fig 5.2 shows the dark conductance of the sample plotted against reciprocal temperature from which the sample was first annealed to 430 K for 30 min, and then cooled to room temperature. We then heated the sample again and measure the conductance at different temperatures. From the Fig 5.2, the conductance of the sample have two different slopes. The kink temperature is about 340 K. This is caused by the thermal equilibration effect.

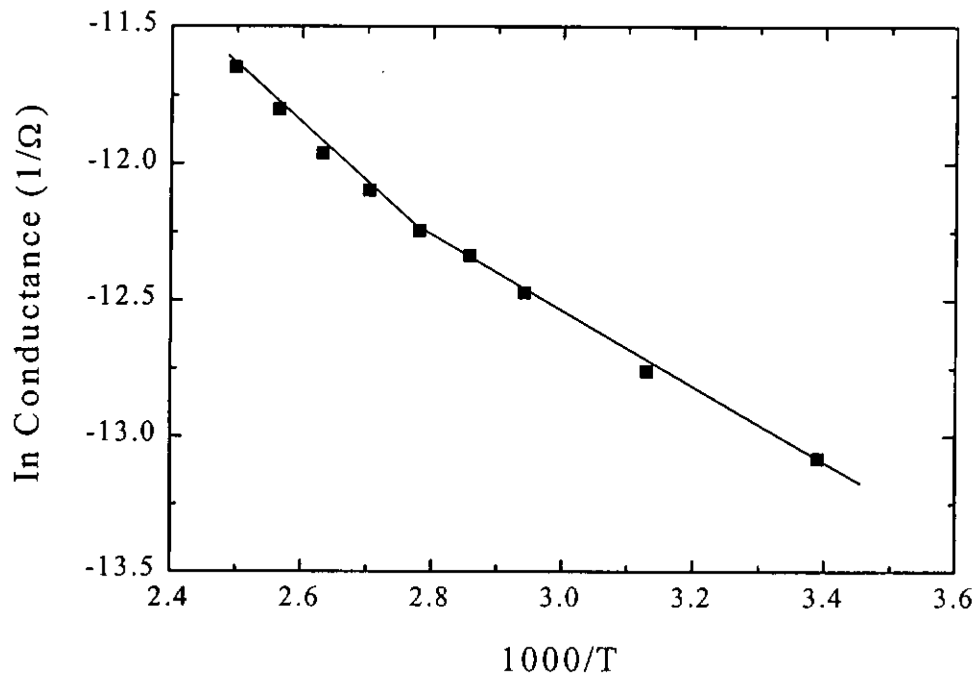

Figure 5.2: The temperature dependence of conductance.

2 Low-frequency noise and Thermal equilibration effect

The basic model of the noise relates the frequency and the bias current to the observed noise power spectral density. This is described by the expression :

$$S_n(f) = K\frac{I^b}{f^\gamma} \tag{5.1}$$

where $S_n(f)$ is the power spectral density function of the noise, I is the bias current, f is the frequency and K is a constant which may depend on other factors such as temperature and the history of the sample. The exponents b and γ are experimentally determined parameters.

Fig 5.3 shows typical noise spectra over a spectral window of 80 Hz to 1080 Hz for the sample at five different biasing conditions : $7\mu A$, $9\mu A$, $11\mu A$, $13\mu A$ and $15\mu A$ at room temperature. The noise power spectra is increased as the bias increase. By fitting the spectrum by linear regression, the slope of spectrum is $\gamma = 1$. Therefore, the device is producing $1/f$ fluctuations within this range of frequency.

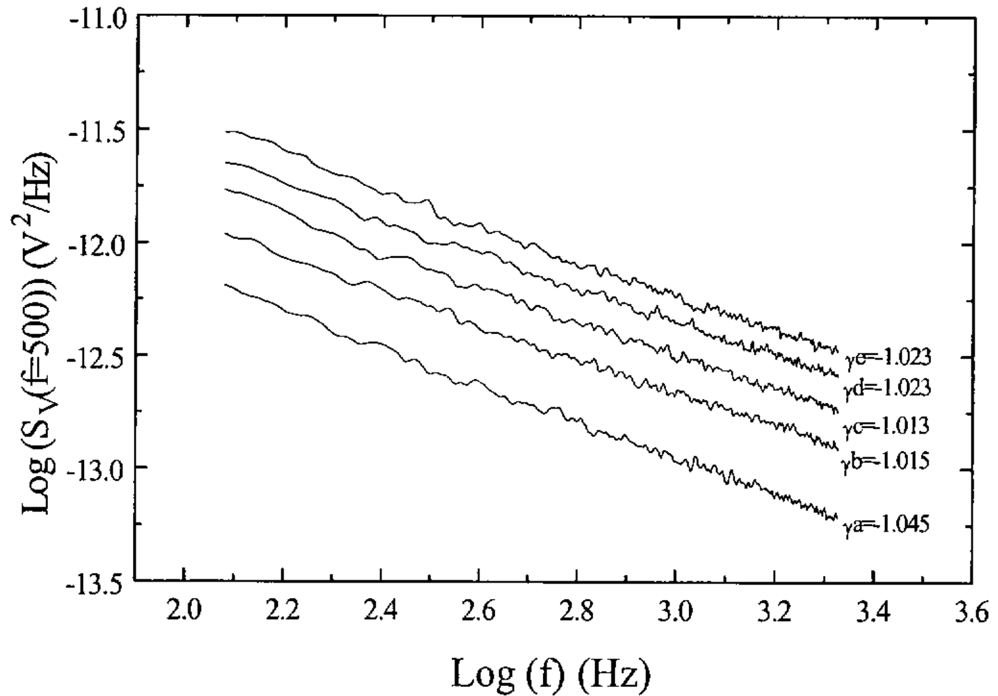

Figure 5.3: The noise power spectrum for five different current bias : a=$7\mu A$, b=$9\mu A$, c=$11\mu A$, d=$13\mu A$ and e=$15\mu A$ at room temperature.

The parameter, b, in Eq: 5.1 is used to determine the linearity of the noise. A linear noise relationship would exist if the exponent b is equal to 2 since the equation is given in terms of noise power. The research group of Parman and Kakalios[3] had observed the non-linear behavior of $1/f$ noise in *a-Si:H* films with sub-linear characteristic $b \approx 1$ at low temperature and super-linear behavior ($b \approx 2.5$) at high temperature. These results

were unexpected and quite interesting leading them to further investigations of the origin of the noise. Fig 5.4 shows the noise power for 200 Hz as a function of the bias current. Linear fits to the power law $S_n \propto I^b$ with b $\simeq$ 1.56. This result is consistent with previous result that the noise power spectra of the *a:Si-H* is exhibit a non linear behaviors.

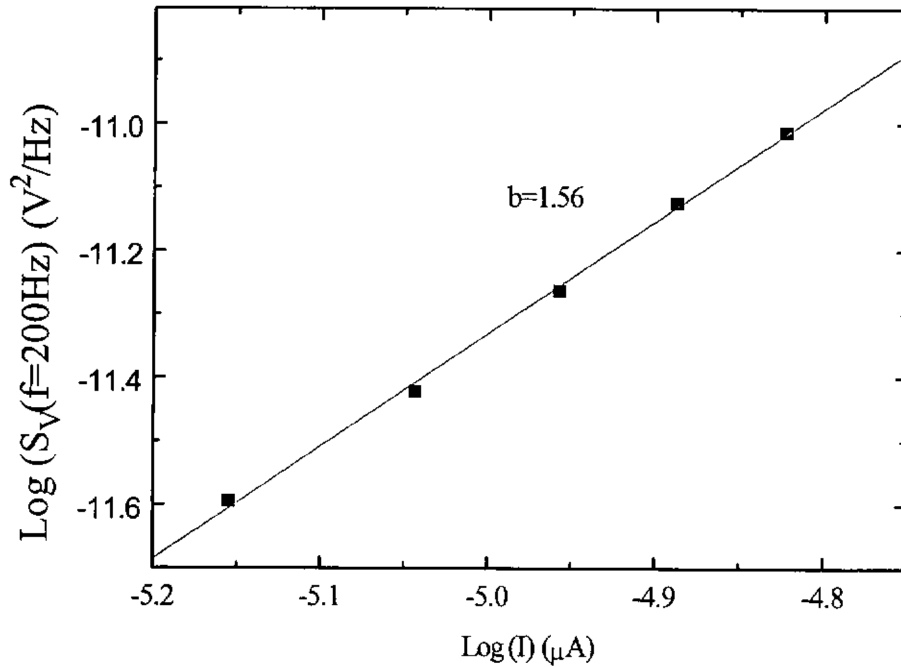

Figure 5.4: The noise power for 200 Hz as a function of the bias current.

Fig 5.5 shows the noise power spectra at 300 K, 360 K and 430 K. The data clearly shows that the decrease of the entire spectrum as the temperature is increased.

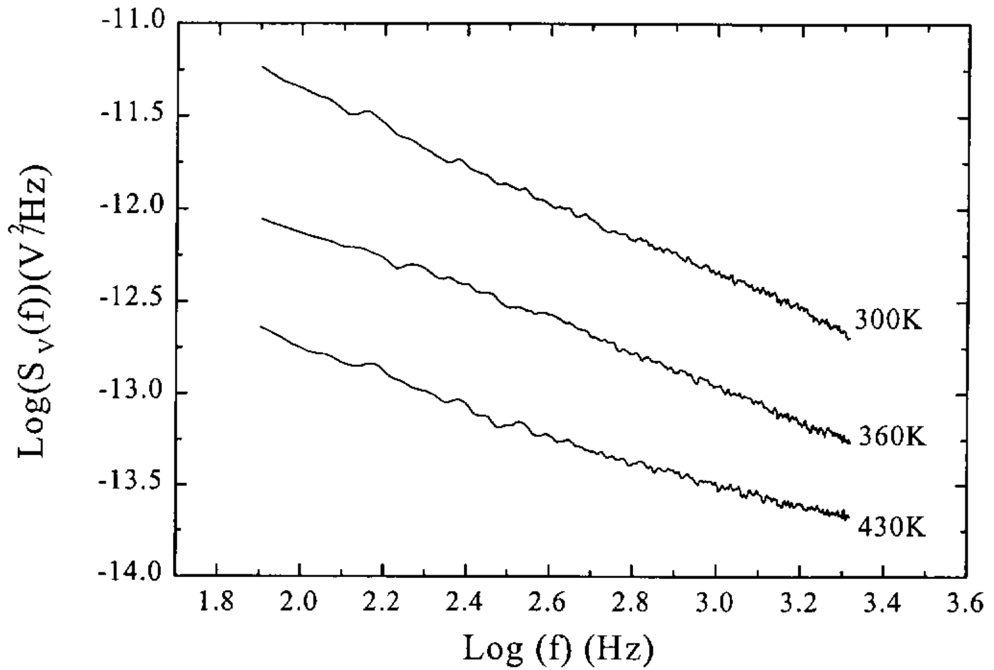

Figure 5.5: The noise power spectrum as a function of frequency for three different temperatures.

The temperature dependence of the conductivity demonstrate typical thermal equilibration effects of a-Si:H thin films. Following the rapid cooling process, a kink is observed in the Arrhenius plots of the conductivity. Typical result is shown in curve A of Fig 5.6 in which a kink is seen at 380 K. The kink can be removed by annealing the device at 450 K in nitrogen ambient followed by the slow cooling process as indicated in curve A of Fig 5.7. We also observe that there is a shift in the equilibration temperature, T_E, to 350 K.

The Arrhenius plot of $S_V(f = 200Hz)$ for the device after the rapid-cooling-process is shown in curve B of Fig 5.6. The data clearly exhibit two different regimes separated

by a kink at about 380 K. Again, there is a strong correlation between the temperature dependencies of the device conductance and the voltage noise power spectra. The kink in the voltage noise power spectra can also be removed by the slow cooling process. The result is shown in curve B of Fig 5.7. Similar to the conductance data the voltage noise power spectra for samples that under slow cooling process exhibit a lower equilibration temperature at 350 K. Figures 5.6 and 5.7 clearly demonstrate a close correspondence between the temperature dependencies of the conductance and the voltage noise power spectra.

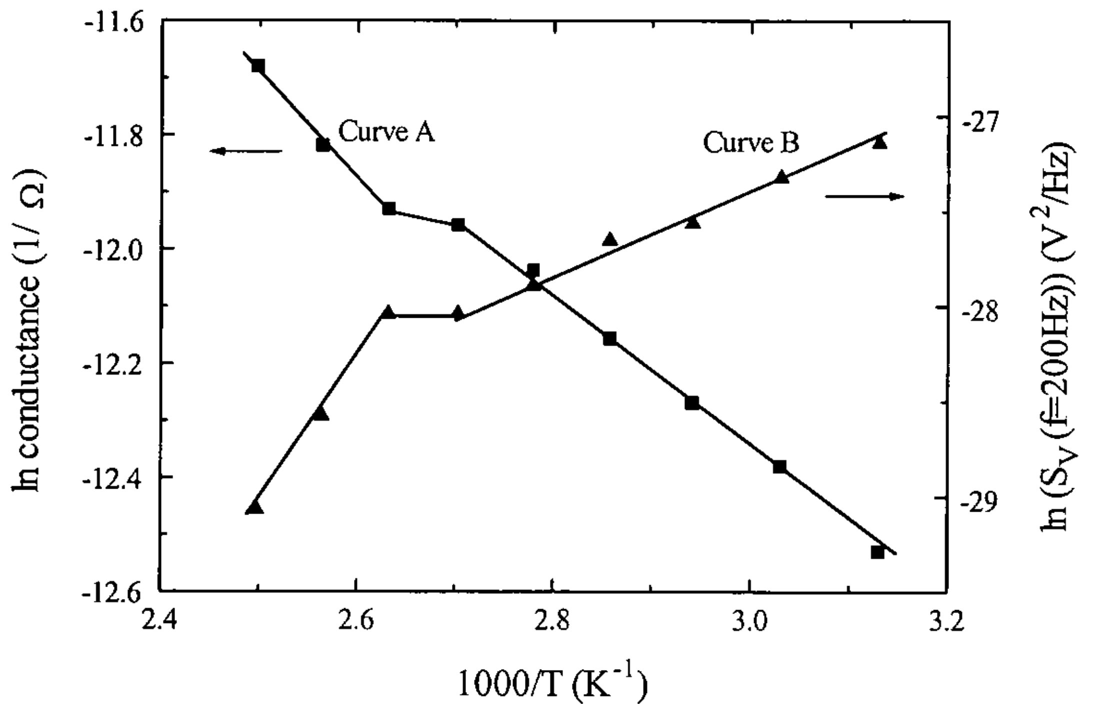

Figure 5.6: The Arrhenius plots of the conductance (curve A) and the voltage noise power spectral density measured at 200 Hz (curve B) after annealing followed by the rapid-cooling process.

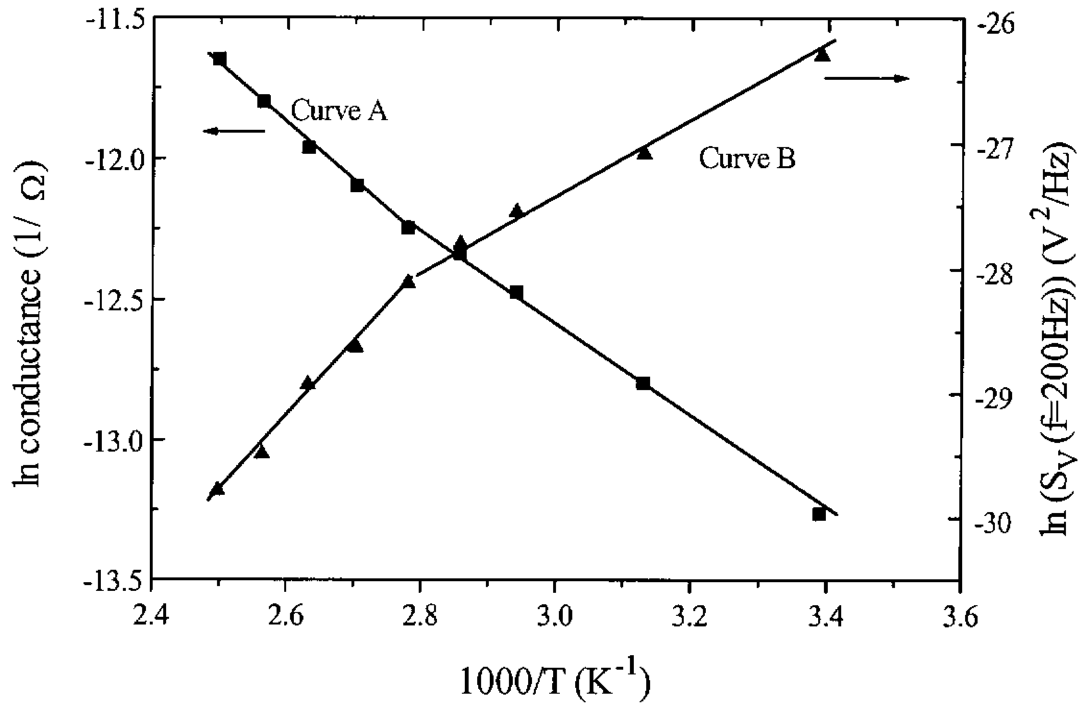

Figure 5.7: The Arrhenius plots of the conductance (curve A) and the voltage noise power spectral density measured at 200 Hz (curve B) after annealing followed by the slow-cooling process.

3 Results of low-frequency noise and light induced metastability in *a-Si:H* films

The time dependence of conductance for light induced metastable effect for which the sample was exposed to 500 W Xe lamp with an AM0 filter placed between the sample and the lamp is shown in Fig 5.8. When the sample was exposed to Xe lamp, it exhibited a persistent conductivity effect in which the conductance increased with exposure time, which is shown in, curve A. Curve B shows that after exposure, the conductance of the sample decreased slowly. However, within the duration of our experiment, the conductance appeared to settle at a value higher than the pre-exposure value. This is an indication of structural change in the material due to Xe lamp exposure.

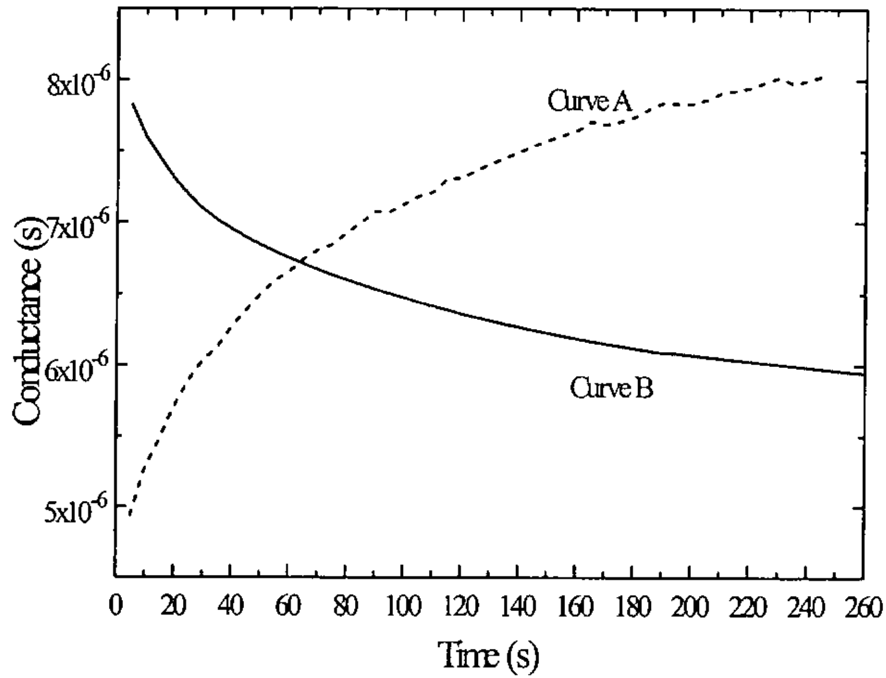

Figure 5.8: The time dependence of conductance. Curve A shows the conductance of the sample during exposure to Xe lamp. Curve B shows the conductance of the sample after exposure.

To study this effect, we investigate the time dependence of the noise power spectral density due to light illumination. The device was placed in a sample holder which is shown in Fig 4.1. The conductance and the low frequency noise of the sample were measured before exposure to Xe lamp. Then the sample was exposed to Xe lamp with AM0 filter for 1 hour. The conductance and the noise power spectra were measured after each hour. The normalized noise power spectral density at 500 Hz before exposure is about -14.54. After the sample was exposed to Xe lamp, the noise power spectral density at 500 Hz is found to be around -14.42 as shown at Fig 5.9. The conductance of the sample before exposure is about 4.9×10^{-5}. The conductance increased to 6.5×10^{-5} upon Xe lamp illumination for 1 hour and upon turning off the light source, the conductance slowly deceased to 6.0×10^{-5} over a period of 25 hours as shown in Fig 5.10.

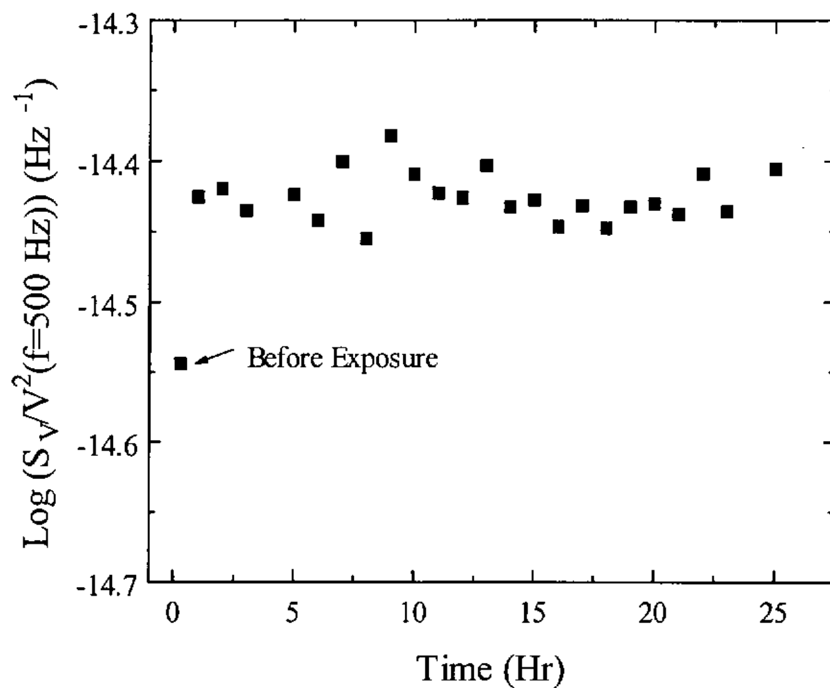

Figure 5.9: The time dependence of noise power spectral density at 500 Hz for the sample after exposure to Xe lamp.

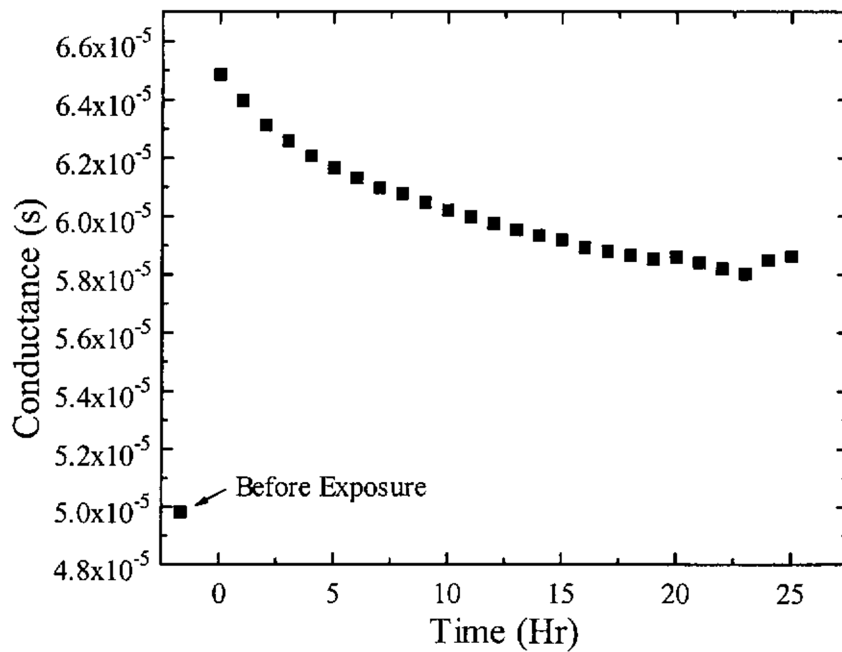

Figure 5.10: The time dependence of conductance for the sample after exposure to Xe lamp.

The exposure time dependence of conductance for the sample exposed to 10 mW cw HeCd laser illumination is shown in Fig 5.11. It also shows a persistent conductivity effect, that the conductance increases with exposure time. When we stop the light exposure, the conductance remains at this level. However, the exposure time dependence of normalized noise power spectra for laser induced metastable effect is shown in Fig 5.12. It shows that the normalized noise decreases as a function of exposure time at the beginning and smooth out at the end.

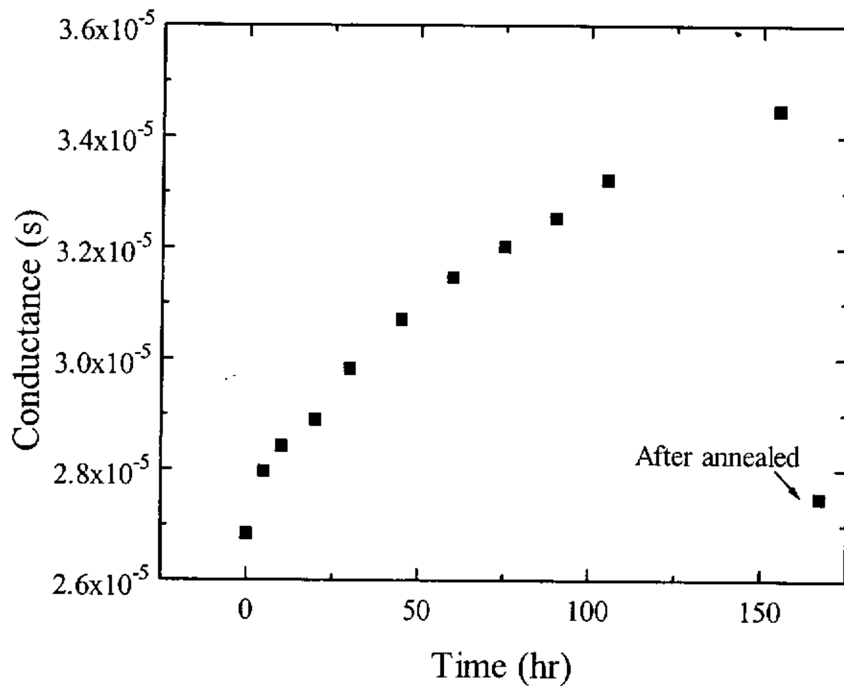

Figure 5.11: The exposure time dependence of conductance for the sample after exposure to HeCd laser illumination.

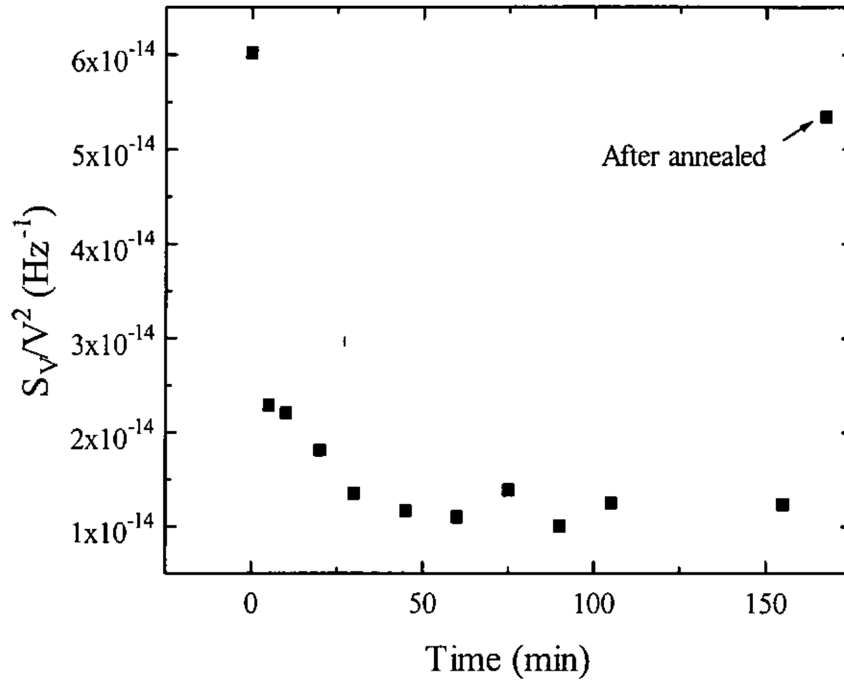

Figure 5.12: The exposure time dependence of noise power spectral density at 500 Hz for the sample after exposure to laser illumination.

To further investigate light induced metastability in *a:Si-H*, we conduct fourier transform infrared spectroscopy (FTIR) and positron annihilation spectroscopy (PAS) to examine structural change in *a:Si-H* films. The IR transmission spectra for *a-Si:H* films exposed to Xe lamp illumination is shown in Fig 5.13. The sample was first annealed at 450 K and then cooled with a slow cooling rate of $0.02°C/s$ and then exposed to Xe lamp illumination. The IR transmission was decreased. The peak correspond to resonance frequencies for SiH@(900cm^{-1}) and SiH_3 (2000cm^{-1}) bonds. But it does not change as a function light illumination. The decrease in the other peaks means that the number of silicon-hydrogen bonds increased after the sample was exposed to Xe lamp illumination. The IR transmission spectra for the *a-Si:H* film, which was exposed to 10 mW HeCd laser illumination, is shown in Fig 5.14. The IR transmission spectra was also decreased when the sample was exposed to laser illumination. The decrease in IR spectra for the

sample exposed to Xe lamp illumination was larger than the one exposed to laser illumination. It means that the increase in the number of silicon-hydrogen bond due to Xe lamp illumination was much more than the one exposed to HeCd laser illumination.

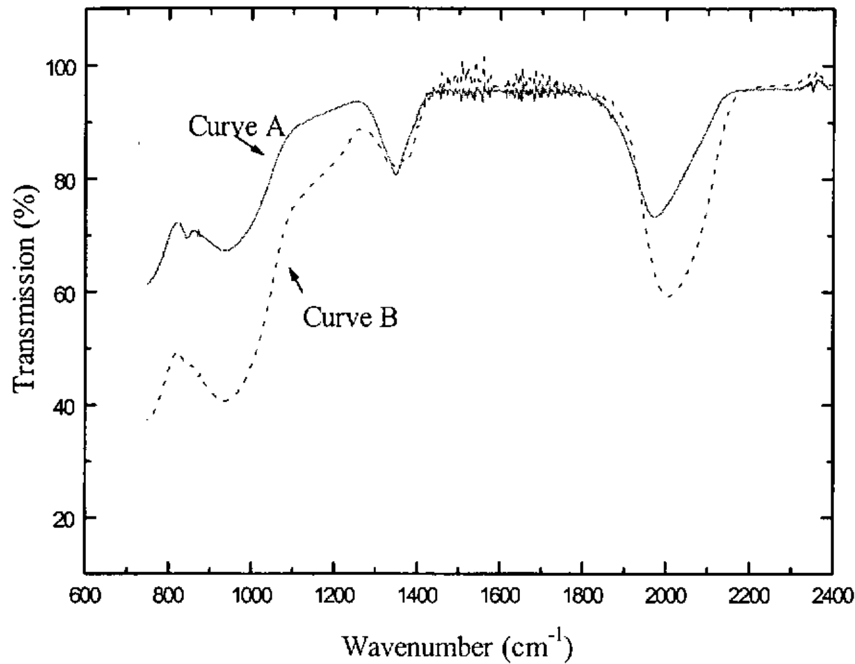

Figure 5.13: IR transmission spectra for *a-Si:H* samples after annealing at 450 K (Curve A) and after the sample was exposed to Xe lamp illumination (Curve B).

For the PAS measurement, the S parameter is used to charactize the defects in the material. Large S parameter means more defect states in the material. The S parameters for both samples subject to Xe lamp and HeCd laser illumination are shown in Figs 5.15 and 5.16. For the sample exposed to Xe lamp illumination, the S-parameter was decreased. After re-annealing it to 450 K, there was little further change in S-parameter. For the sample exposed to HeCd laser illumination, a decrease in the S-parameter was observed after initial HeCd laser illumination. As opposed to Xe lamp illumination further decrease in the S parameter was observed upon re-annealing the sample at 450 K.

The results are consistent with the FTIR spectra. When *a-Si:H* films were exposed to either Xe lamp or laser illumination, there was an increase in the number of Si-H bonds leading to a decrease in defect density. Similar results have been observed by Qing Zhang who reported light induced annealing effect in *a-Si:H*. In their studies, they observed significant annealing of *a-Si:H* bonds upon exposed to Xe lamp illumination.

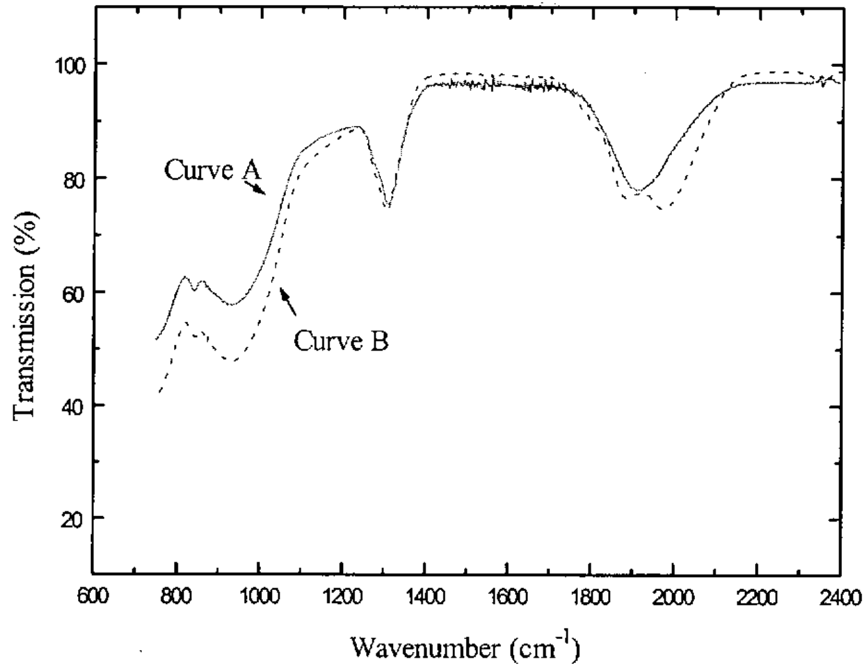

Figure 5.14: IR transmission spectra for *a-Si:H* samples after annealed to 450 K (Curve A) and the sample was exposed to laser (Curve B).

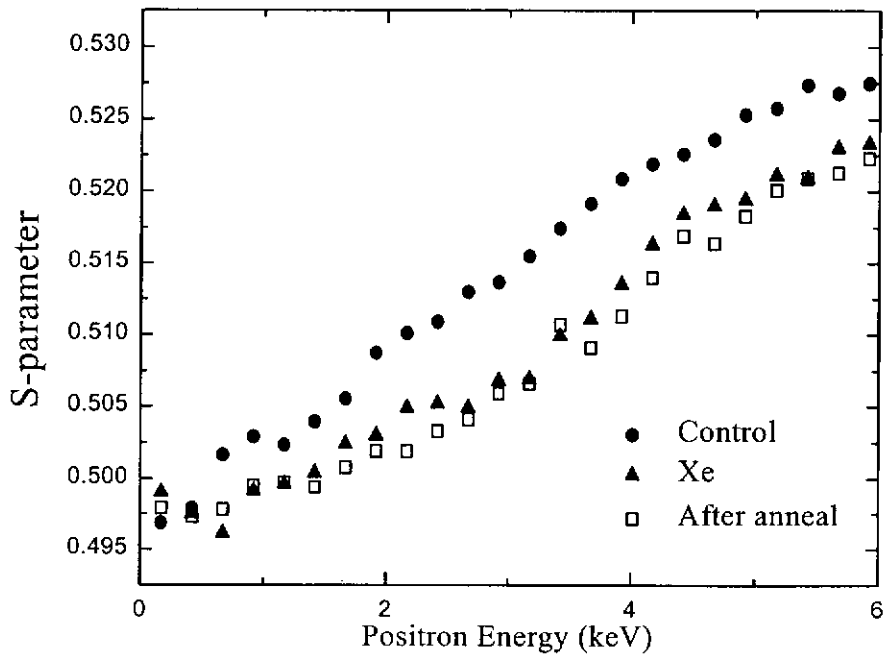

Figure 5.15: S-parameter (S(E)) for the sample before exposed, after exposed, and annealing after exposed to Xe lamp.

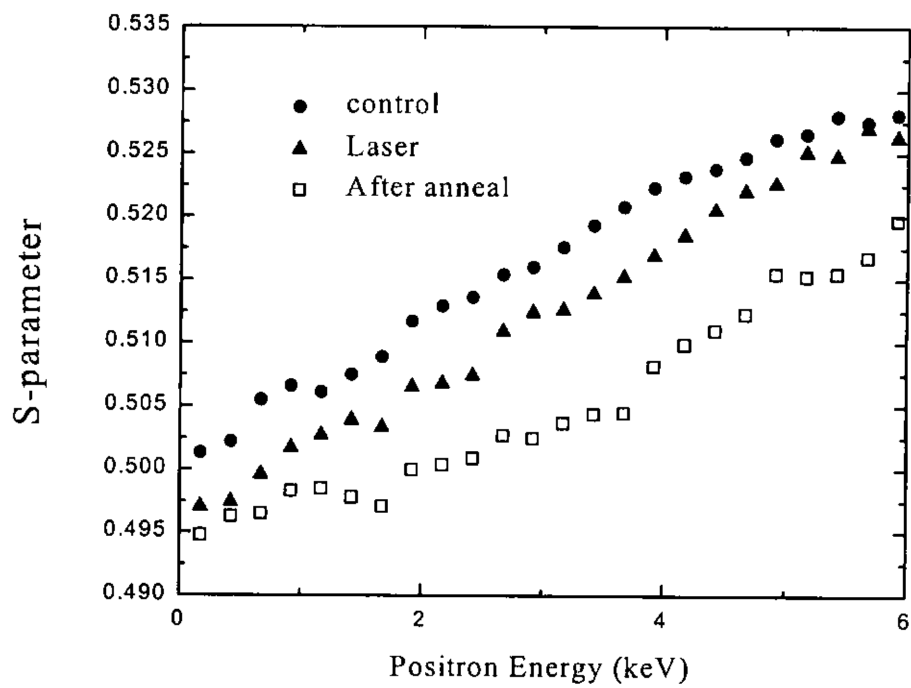

Figure 5.16: S-parameter (S(E)) for the sample before exposed, after exposed, and annealing after exposed to HeCd laser.

Chapter 6

Discussion

1 Thermal equilibration effect

Studies on the structural and electronic properties of *a-Si:H* in the past decade have provided evidences for large scale inhomogeneity of the material in structure, Coulomb potentials and hydrogen distribution. These lead to long range fluctuations in the potential within the material, which directly affects the local energy of the mobility edge. The non-uniformity of hydrogen distribution exists in the form of a sub-matrix of hydrogen network in the *a-Si:H* material and hydrogenated voids, in which large hydrogen concentration is found around the voids. These cause the band gap to increase in regions with high concentration of hydrogen. Also, carriers depletion are observed in regions with high hydrogen concentration which leads to percolation as one of the means of carrier transport in the medium.

Hydrogen motion is shown to be central to the thermal equilibration of the device conductance. The phenomenon has been widely studied by many researchers in the field. The

results obtained by various groups are very similar to what we observed in our devices. It is shown that the equilibrium distribution of the hydrogen sub-matrix is a function of temperature. In addition, the bonded hydrogen in the *a-Si:H* films demonstrate glassy behavior. At the glass transition temperature there are substantial rearrangements of the structure of the equilibrium hydrogen matrix. The hydrogen matrix for samples that have undergone the rapid-cooling process becomes frozen in a metastable state-giving rise to a kink in the Arrhenius plot of the sample conductance. Whereas for the samples that experienced the slow-cooling process the kink is absent because the structure is maintained at equilibrium down to a lower temperature.

In our investigations of $1/f$ noise in the materials we note the close correspondence between the thermal equilibration of the device conductance and the temperature dependencies of $S_V(f)$, as seen in figures 5.6 and 5.7. This provides strong evidence that the same physical mechanism underlies both phenomena. Also, as hydrogen diffuses through the amorphous silicon it changes the bonding configurations of dopants and silicon atoms as well as the defect and charge distribution. Therefore hydrogen motion results in the change in the local mobility edge leading to the modulation of the percolation path of the carriers.

From the experimental data we observe the deviation of $S_V(f)$ from an I^2 dependence. This signifies the presence of non-linearity in the physical process underlying the low-frequency excess noise. This is consistent to the model postulated by Parman et al., which stipulates that carrier percolation underlies the low-frequency noise in the materials. Previous studies of percolation noise in other systems also exhibit a deviation in I^2

dependencies [6,7].

Based on the above model, we employ the percolation model to examine the result. In a percolation system the resistance R is :

$$R = C(\rho - \rho_c)^{-t} \tag{6.1}$$

where ρ is the filling factor, ρ_c is the critical filling factor, C is a constant and t is the dimensionality of the system. Assuming the fluctuations in R, is due to from fluctuations in ρ,

$$\Delta R = \frac{\partial(\rho - \rho_c)}{\partial \rho}\Delta\rho \tag{6.2}$$

$$\Delta R = -tC(\rho - \rho_c)^{-t-1}\Delta\rho \tag{6.3}$$

Finding the noise power spectrum density by using Wiener-Khintchine theorem. Finally we get:

$$S_R(f) = t^2 C^{-2/t} R^{(2+2/t)} S_\rho(f) \tag{6.4}$$

$$S_V(f) \propto R^p S_\rho(f) \tag{6.5}$$

where $p = 2 + 2/t$

Experimental results are shown in Fig 6.1 and 6.2. Following the rapid cooling process, p changed from 4.1 to 1.5 as T is varied from below to above the kink temperature. After slow cooling process, p is found to change from 2.1 at low temperature to 1.6 at high temperature as shown in Fig 6.2. Such close correspondence between the temperature dependencies of the conductance and the low-frequency noise strongly indicated that the two share the same physical origin. The values of p measured from our data ranged from

1.5 to about 4 which roughly falls within the range of the calculated values. Moreover, the value of p changes as T is varied from below to above the equilibration temperature. We believe that the temperature dependencies arises from the fact that at the glass transition temperature the hydrogen sub-matrix undergoes significant structural changes, which may result in the variation in the fractal dimension of the carrier percolation path which needs to be confirmed by more detailed investigations.

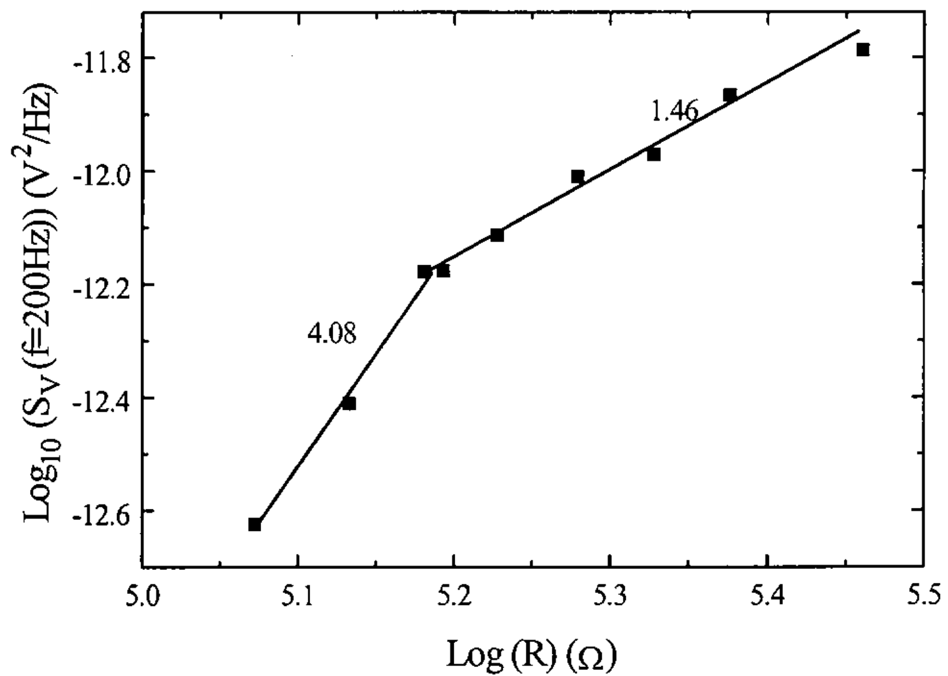

Figure 6.1: $\text{Log}_{10}\ S_V(f = 200Hz)$ vs $\text{Log}_{10}R$. The data are obtained after the device have experienced thermal annealing at 450 K followed by the rapid-cooling process.

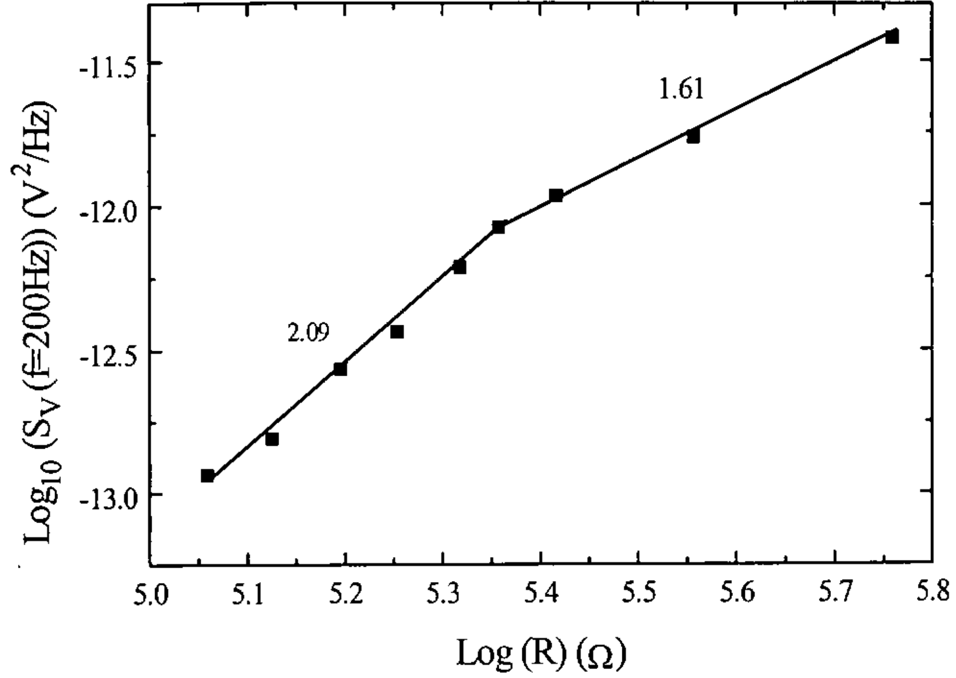

Figure 6.2: $\text{Log}_{10}\ S_V(f = 200Hz)$ vs $\text{Log}_{10}R$. The data are obtained after the device have experienced thermal annealing at 450 K followed by the slow-cooling process.

2 Light induced metastability

From the experimental data of the conductance of the samples exposed to Xe lamp or HeCd laser illumination, we clearly see that the film exhibit persistent photoconductivity effect. Previous experiments suggested that, when *a-Si:H* films were expose to light, hydrogen related bond would be broken, causing an increase in band tail states. The filling of the states causes the Fermi level to move toward the conduction band leading to an increase in conductance. Refer to Hooge's empirical formula:

$$\frac{S_V}{V^2} = \frac{\alpha}{Nf} \tag{6.6}$$

where N is the number of carriers. From the noise results, the noise power spectra decreased when the sample was exposed to both Xe lamp and laser illumination. This agrees well with Eq. 6.6, when a *a-Si:H* film was exposed to the light, the conductivity increases. It reflects on the increase in number of carriers, leading to decrease in the noise power spectra. On the other hand, decrease in the noise seem to be faster than the increase in N as indicated by conductance measurement. Therefore the data suggest that light illumination affects the noise by more than simply changing the carrier concentration. It is likely that structural changing underlies the observed dependence of the noise on light illumination.

Light-induced reversible structural changes in amorphous silicon are poorly understood on a microscopic level. One interesting observation is the apparent saturation in the density of light-induced defects, which has important implications for the origin of the metastability. Such phenomenon was reported by Q. Zhang[54] who observed saturation of light induced defects when *a-Si:H* films were exposed to high intensity light from Xe lamp. Pervious studies[55][56] showed that such an effect many arise from the balancing of the photo-induced defect creation/annihilation process, the Staebler-Wronski effect. This isrepresented by the equation below:

$$SiH \overset{h\upsilon}{\rightleftharpoons} Si + H \qquad (6.7)$$

Experimental evidence for light-induced annealing was demonstrated by Q. Zhang[54] who observed the phenomenon using ESR experiment for undoped *a-Si:H* film subject to photo illumination by Xe lamp at 100°C. Previous research showed that the light-induced annealing of metastable defect was observed in both photoconductivity and electron spin

resonance experiments.

We also observed similar light induced annealing effects in our experiments. We clearly observed an increase in *Si-H* bonds after the sample was illuminated by Xe lamp and HeCd laser. In figs 5.13 and 5.14, we observed a decrease in the IR transmission at wavenumber 2080cm^{-1} and 960cm^{-1}. These valleys corresponds to the resonance frequency of SiH_3 and SiH bonds. A decreasing in the transmission at such frequency indicates an increase in the density of SiH_3 and SiH bonds as a result of Xe lamp and HeCd laser illumination.

Experiments on the PAS of *a-Si:H* films subsequent to Xe lamp and HeCd laser illumination also exhibit similar photo-induced annealing effects in the sample. For Xe lamp illuminated sample, a significant reduction in the S-parameter was observed. As discussed in chapter 2, the PAS is a sensitive tool for characterizing defect densities in *a-Si:H* films. A decrease in PAS indicates a reduction in defect density in the film subsequent to photo-illumination. Such effect was observed for both Xe lamp and HeCd laser illumination samples, indicating light-induced annealing effects in both samples. Moreover, the PAS experiment also showed that upon thermal annealing, there was a further decrease in the S-parameter for the HeCd laser illuminated film. However, little change is observed for the Xe lamp illuminated film. A possible explanation for this effect is that illuminating the film with Xe lamp and HeCd laser have quite different effects on the nature of defects in the sample. At this point, we cannot state clearly that which kind of defect that was involve in light-induced annealing. The doped *a-Si:H* system further complicate the situation. When hydrogen diffuses, it can break Si-H bonds or

form bonds with existing dangling bonds. On the other hand, it also breaks P-H bonds, to make 3 fold inactive doping to 4 fold. This will lead to an increase in band tail state, and increase in conductance. More detailed studies have to be conducted to pin point the exact mechanism of the observed phonomenon.

Chapter 7

Conclusion

We conducted detailed studies of low-frequency noise, Fourier transform infrared spectroscopy (FTIR) and positron annihilation spectroscopy (PAS) to characterize the metastability in n-type *a-Si:H*. The experiments were divided into two part. First part is to characterize the thermal equilibrium of *a-Si:H*. The noise power spectrum was measured from room temperature to about 420 K. The device was first annealed at 450 K and then cooled to room temperature at a rate of 0.5 K/s. The voltage noise power spectra and the conductance of the device were characterized from room temperature to 420 K. The experiment was then repeated with the device annealed again and subsequently cooled at a rate of 0.02 K/s. The Arrhenius plots of the voltage noise power spectrum, $S_V(f)$, were found to exhibit thermal equilibration processes commonly observed in *a-Si:H* materials. Characterization of the bias dependencies of the noise show that $S_V(f)$ deviates from an I^2 dependence indicating that the noise arises from a non-linear process. Also, $S_V(f)$ is proportional to R^p where p is dependent on the temperature and the cooling process of the device. Our experimental data provide strong evidence that the

flicker noise originates from hydrogen motion within the material. The process appears to cause fluctuations in the device conductance by modulating the percolation path of the carriers.

The second part of the experiment is to characterize the light induced metastability in *a-Si:H* thin film. The device was first annealed at 450 K and then cooled to room temperature at a rate of 0.02 K/s. Then sample was exposed to the Xe lamp illumination with AM0 and AM1 filter. The voltage noise power spectra and the conductance of the device was characterized with time. Another sample was exposed to HeCd laser illumination. After each 15 min exposure, the voltage noise power spectra and the conductance of the device was measured. Device conductance increased after illumination by either light sources. It was suggested that the material exhibits persistent conductivity in which the broken hydrogen related bond such as P-H bond and result in increase in occupied band tail state. From the noise experimental result for the sample exposed to laser. Decrease in noise seem to be faster than in increase in N as indicated by conductance measurement. Therefore the data suggest that light illumination affect the noise more than just changing the carrier concentration. Further experiment was performed to examine the effect of light illumination. From the results of FTIR and PAS experiments result, the defect density of the sample decreased after illumination. This suggests that illumination not only leads to persistent conductivity but also lead to light induced annealing. More detailed investigations are needed to explain the physical mechanism.

Bibliography

[1] Spear, W.E and LeComber, P.G. Solid State Comm. **17**, 1193 (1975).

[2] Brodsky, M.H. and Title, R.S., Phys Rev. Lett. **23**, 581 (1969).

[3] C.E. Parman, N.E. Israeloff, and J. Kakalios, Phys. Rev. **B47**, 12578 (1993).

[4] C.E. Parman, N.E. Israeloff, and J. Kakalios, Phys. Rev. **B44**, 8391 (1991).

[5] C.E. Parman, N.E. Israeloff, and J. Kakalios, Phys. Rev. Lett. **69, 1097** (1992).

[6] H. Wieczorek, J. Appl. Phys. **77**, 3300 (1995).

[7] L.M. Lust and J. Kakalios, Proceedings of Mat. Res. Soc. Vol. **377**, 401 (1995).

[8] P.H. Leo, K.D. Moore, P,L, Jones, and F.H. Cocks, Phys. Status Solidi B **108**, K145 (1981).

[9] A. Papuulis, Probability, random variables and stochastic process, McGraw-Hill, New York (1965).

[10] A. van der Ziel, Noise in solid state devices and circuits, Wiley: New York (1986)

[11] A. van der Ziel and E.R. Chenette, "Noise in solid state devices," in Advances in Electronics and Electron Physics, ed. L. Marton, (Academic Press, 1987) vol. 49, p.225.

[12] P. Dutta and P.M. Horn, "Low-frequency fluctuations in solids: 1/f noise," Rev. Mod. Phys., vol. 53, pp.497-516 (1981).

[13] F.N. Hooge, T.C. M. Kleinpenning, and L. K. J. Vandamme, Rep. Prog. Phys., vol. 44, p. 31 (1981)

[14] M. B. Wessman, "1/f noise and other slow, nonexponential kinetics in condensed matter," Rev Mod. Phys., vol. 60, pp. 537-571 (1988)

[15] A. Van der Ziel, "Unified presentation of 1/f noise in electronics devices: fundamental 1/f noise sources," Proceedings of the IEEE vol. **76**, pp. 233-258 (1988).

[16] C.M. Van Vliet, "A survey of results and future prospects on quantum 1/f noise and 1/f noise in general," Solid-State Electron., vol. **34**, pp. 1-21 (1991).

[17] F.N. Hooge and A.M.F. Hoppenbrouwers, Physica, vol. **45**, 386 (1969).

[18] F.N. Hooge and L.K.J. Vandamme, Phys. Lett. A, vol. **66**, 315 (1978).

[19] R.P. Jindal and A. van der Ziel, J. appl. Phys., vol. **52**, 2884 (1981).

[20] P.H. Handel, Phys. Rev. Lett., vol. **34**, 1492 (1975).

[21] G.S. Kousik, C.M. Van Vliet, G. Bosman, and P.H. Handel, Adv. Phys., **34**, 663 (1985).

[22] G. Bosman, M.Y. Luo, A. van der Ziel, and L.L. Hensch, IEEE Trans. Electron Devices, **35**, 261 (1988).

[23] P.H. Handel, in Proc. 7th Int. Conf. Noise in Physical Systems and 3rd Int. Conf. On 1/f Noise, ed. M. Savello, G. Lecoy, and J.P. Nougier, (Montpellier, 1983), 97.

[24] F.N. Hooge, Proceedings of the International Conference on Noise in Physical Systems and 1/f Fluctuations, ed. T. Musha, S. Sato and M. Yamamoto, (Kyoto, Japan, 1991).

[25] J. Bernamont, "Fluctuations de potenial aux brones d'un conducteur metalliaque de faibe volumne parcouru par un courant," Ann. Phys., **7**, 71 (1937).

[26] M.M. Surdin, J. Phys. Radium, **10** 188 (1939).

[27] A.L. McWhorter, Ph. D. Thesis, MIT, Lincoln Lab. Technical Report Pulb. 80 (1995).

[28] S. Christensson, I. Lundstrom, and C. Svensson, Solid-State Electron., **11**, 797 (1968).

[29] Charles Surya and Thomas Y. Hsiang, Phy Rev. B **33**, 4898 (1986).

[30] Perkowitz, S and Thorland R. H., Phy. Rev. B **9**, 545 (1974).

[31] Kim, O. K. and Spitzer, W. G., Phy. Rev. B **20**, 3253 (1979).

[32] W. Trifthauser and G. Kogel, Phys. Rev. Lett., **48**, 1741 (1982).

[33] S. Berko and J.C. Erskine, Phys. Rev. Lett., **19**, 307 (1967).

[34] I.K. MacKenzie, T.L. Khoo, a.B. McDonald, and B.T.A. McKee, Phys. Rev. Lett., bf 19, 946 (1967).

[35] Positron Solid State Physics, Proceedings of the Internalional School of Physics "Enrico Fermi," Course LXXXIII, Varena, 1981, edited by W. Brandt and A. Dupasquier (Northe Holland, Amsterdam, 1983).

[36] W. Cherry, Ph. D. dissertation, Princeton University, 1985.

[37] B.Y. Tong, Phys. Rev. **B 5**, 1436 (1972).

[38] K.F. Canter, P.H. Lippel, W.S. Crane, and A.P. Mills, Jr., in Positron Studies in Solids, Surfaces, and Atoms, edited by A.P. Mills., W.R. Crane, and K.F. canter (World Scientific, Singapore, 1984).

[39] A.P. Mills, Jr., Appl. Phys., **23**, 189 (1980).

[40] S. Valkealahti and R.M. Chilton, and P.G. Coleman, Appl. Phys. Lett. **59**, 164 (1991).

[41] Staebler, D.L. and Wronski, C.R., Appl. Phys. Lett., **31**, 292 (1977).

[42] R.A. Street and D.K. Biegelsen and J. Stuke, Philos. Mag., **B40**, 451 (1979).

[43] U. Voget-Grote, W. Kummerle, R. Fischer, and J. Stuke., Philos. Mag., **41**, 127 (1980).

[44] W.M. Pontuschka, W.E. Carlos, P.C. taylor, and R.W. Griffith, Phys. Rev. **B25**, 4362 (1982).

[45] D.E. Carlson, Appl. Phys., **A41**, 305 (1986).

[46] J.I. Pankove, and J.E. Berkeyheiser, Appl. Phys. Lett. **31**, 705 (1980).

[47] H. Sersh, J. Stuke and J. Beichler, Appl. Phys. Lett., bf 38, 456 (1980).

[48] M. Stutzmann, Philos. Mag., **B56**, 63 1987.

[49] S. Pantelides, Phys. Rev Lett., **58**, 1344 (1987).

[50] W.B. Jackson and J. Kakalios, Phys. Rev. **B37**, 1020 (1988).

[51] D.G. Ast and M.H. Brodsky, Proc of 14th Intl. Conf. On the Physics of Semiconductors, ed by B.L.H. Wilson. Inst. Phys. Conf. Ser no. 43, p. 159.

[52] R.A. Street, J. Kakalios, and T.M. Hayes, Phys Rev., **B34**, 3030 (1986).

[53] R.A. Street, J. Kakalios, C.C. Tsai and T.M. Hayes, Phys. Rev. **B35**, 1316 (1987).

[54] Qing Zhang, Takayiki Nishino, Minoru Kumeda and Tatsuo Shimizu, Jpn. J. Appl. Phys., **34**, 483 (1995).

[55] R.H. Bube and D. Redfield, J. Appl. Phys., **66**, 820 (1989).

[56] Z.Y. Wu, J.M. Siefert and B.Equer, J. Non-Cryst. Solids **137/138**, 227 (1991).